Old Dog, New Trick: Discovery of the Solid-State Phthalate Detection Capabilities of Fluorescein.

Pablo Labra-Vázquez[a], Marie Gressier[a], Guillaume Rioland[b], Marie-Joëlle Menu[a*]

[a] *CIRIMAT, Université Toulouse 3 Paul Sabatier, Toulouse INP, CNRS, Université de Toulouse, 118 Route de Narbonne, 31062, Toulouse, Cedex 9, France.*
[b] *Centre National d'Etudes Spatiales, DTN/QE/LE, 31401, Toulouse, France.*

Index

S1. General Remarks

All the starting materials were obtained from commercial sources and used without further purification. Infrared spectra were recorded on a Perkin Elmer Spectrum 100 FT-IR spectrometer using a diamond ATR. Elemental analyses were performed at Laboratoire de Chimie de Coordination (LCC) using a Perkin Elmer 2400 series II Instrument. UV-visible and fluorescence spectra in solution were obtained using optical grade solvents and registered at 298 K on Hewlett Packard 8454A and Jobin Yvon Fluoromax 4 spectrophotometers, respectively. Thermogravimetric analyses were carried out ATG/DSC1 Mettler Toledo apparatus under Air with a temperature gradient of 5 °C per minute in a 20-300 °C interval.

S2. Electrochemistry

Electrochemical measurements were carried out with a potentiostat Autolab PGSTAT100. Experiments were performed at room temperature in a homemade airtight three-electrode cell connected to a vacuum/argon line. The reference electrode consisted of a saturated calomel electrode (SCE) separated from the solution by a bridge compartment. The counter electrode was a platinum wire of ca 1cm² apparent surface. The working electrode was a glassy carbon microdisk (1 mm diameter, Bio-logic SAS). The supporting electrolyte (nBu_4N)[PF_6] (Sigma-Aldrich, 99% puriss electrochemical grade) was used as received and simply degassed under argon. The solutions used during the electrochemical studies were typically 10^{-3} M in the compound and 0.1 M in the supporting electrolyte. Before each measurement, solutions were degassed by bubbling Ar, and the working electrode was polished with a polishing machine (Presi P230).

Redox potentials were determined at the inflection points ($E_{ox/red}^{(i)}$) of the first reduction/oxidation waves. To circumvent uncertainty arising from the non-reversibility of certain redox waves, these values were systematically extracted from the second derivative of the CV plots as described elsewhere [1] and used on Equations 1 and 2 to estimate the energy of the FMOs ($E_{HOMO/LUMO}^{CV}$) for these molecules. [1-2] Individual CV plots are presented in Figures S1-S6.

$$E_{HOMO}^{CV}\ (eV) = -(E_{ox}^{(i)} + 4.4) \quad (1)$$

$$E_{LUMO}^{CV}\ (eV) = -(E_{red}^{(i)} + 4.4) \quad (2)$$

It should be noted that some values energies could not be obtained electrochemically, as the oxidation potential of **DEHP** lay outside the electrochemical window of acetonitrile. Additionally, the CV analysis for **FL** (see Figure S6) yielded values for the frontier orbitals (E_{HOMO}^{CV} = -5.76 and E_{LUMO}^{CV} = -3.42 eV) that were inconsistent with the predicted values and incompatible with the optical properties of this tautomer of fluorescein, as discussed in further detail later in the text. Furthermore, these values are too distant from those predicted by DFT. Indeed, the recorded reduction potential is similar to that reported for fluorescein in aqueous NaOH, with a peak at approximately -1.28 V (vs.

SCE).[3] Given that fluorescein exists as a deprotonated species in such basic conditions, it is plausible that our data, obtained in acetonitrile, reflects the presence of deprotonated fluorescein species generated during the CV measurements.

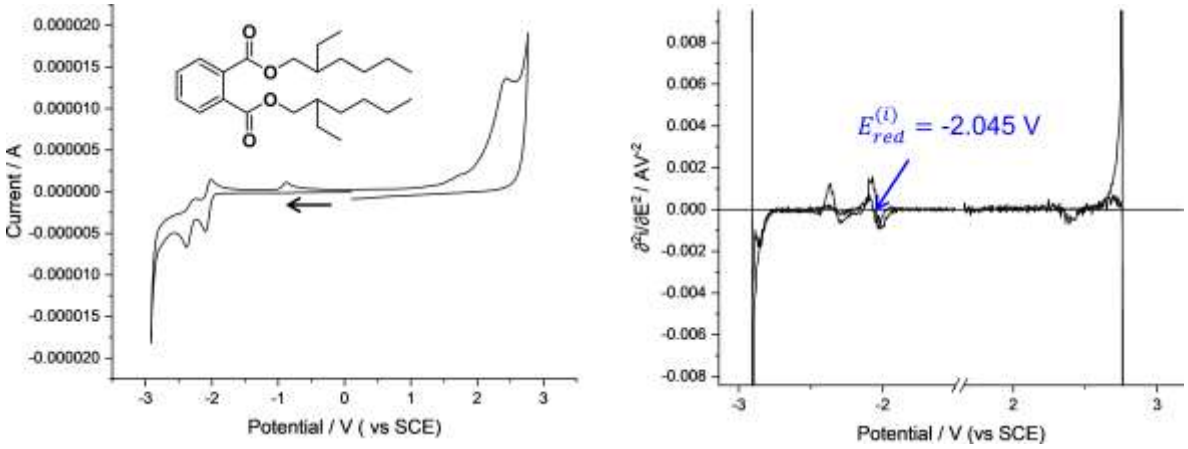

Figure S1. Cyclic voltammetry of di(2-ethylhexyl) phthalate (**DEHP**) on a glassy carbon electrode in acetonitrile + 0.1 mol L^{-1} of (nBu_4N)[PF_6])at 0.1 V s^{-1} (left); redox potentials at the inflection points are indicated on the corresponding second derivative plot (right).

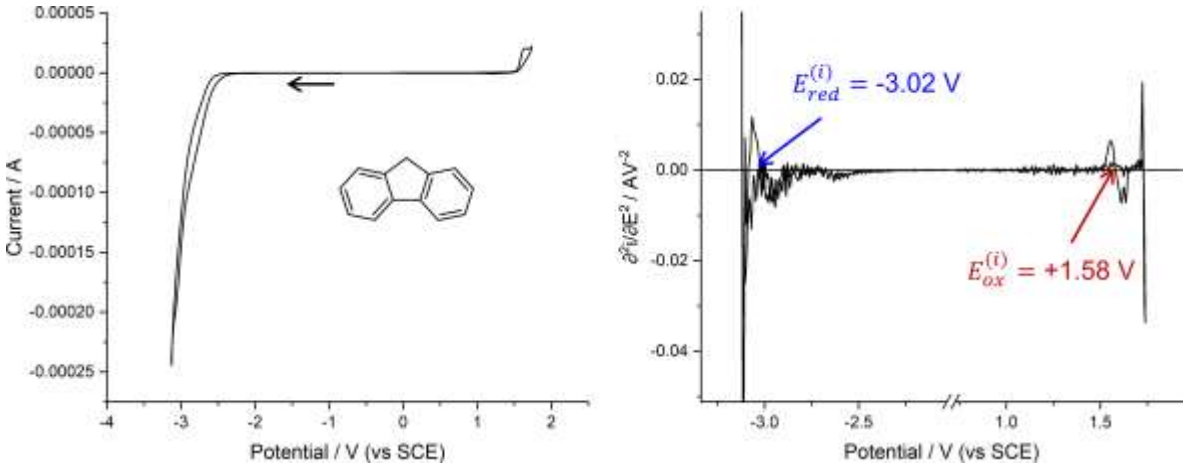

Figure S2. Cyclic voltammetry of 9*H*-fluorene (**F**) on a glassy carbon electrode in acetonitrile + 0.1 mol L^{-1} of (nBu_4N)[PF_6])at 0.1 V s^{-1} (left); redox potentials at the inflection points are indicated on the corresponding second derivative plot (right).

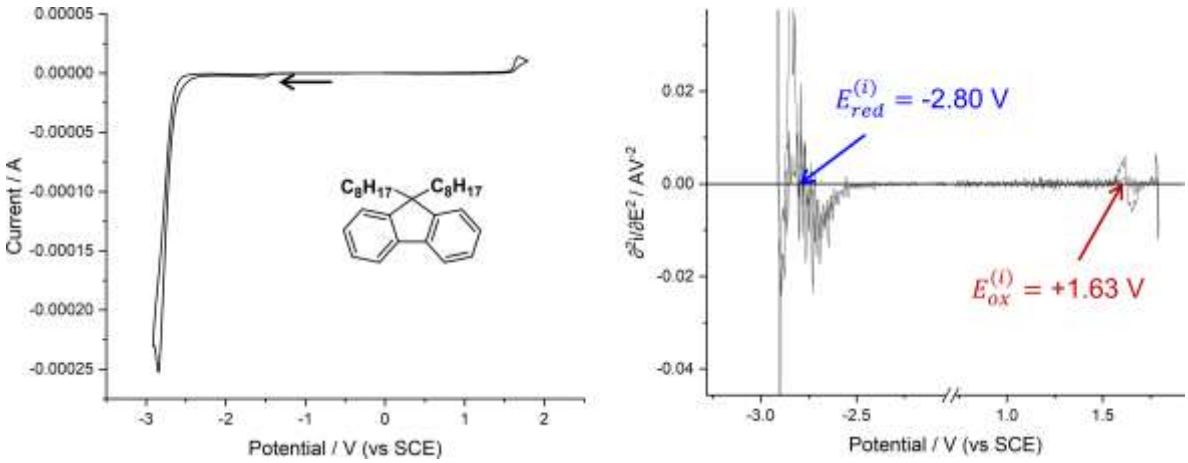

Figure S3. Cyclic voltammetry of 9,9-dioctylfluorene (**FO**) on a glassy carbon electrode in acetonitrile + 0.1 mol L^{-1} of (nBu_4N)[PF_6])at 0.1 V s^{-1} (left); redox potentials at the inflection points are indicated on the corresponding second derivative plot (right).

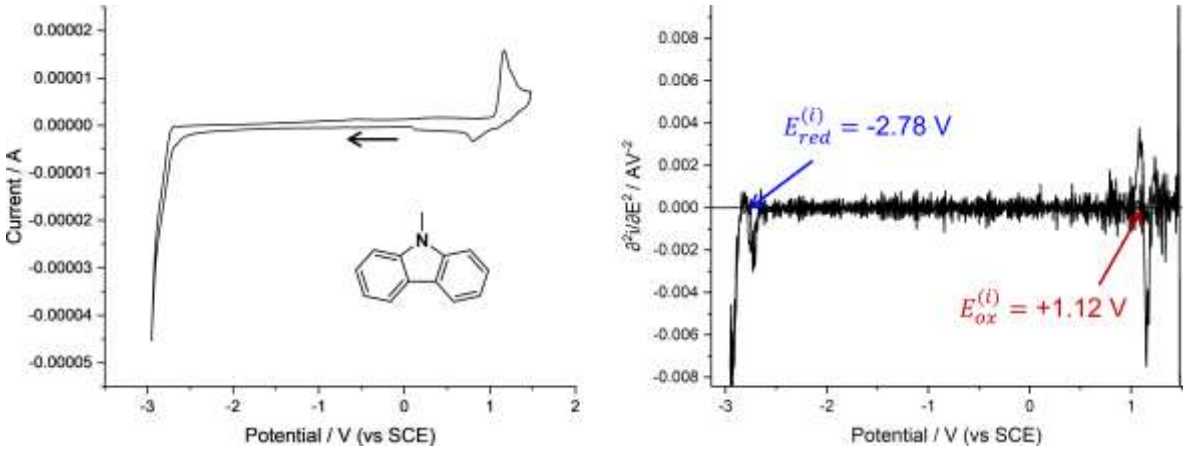

Figure S4. Cyclic voltammetry of 9-methylcarbazol (**C**) on a glassy carbon electrode in acetonitrile + 0.1 mol L^{-1} of (nBu_4N)[PF_6])at 0.1 V s^{-1} (left); redox potentials at the inflection points are indicated on the corresponding second derivative plot (right).

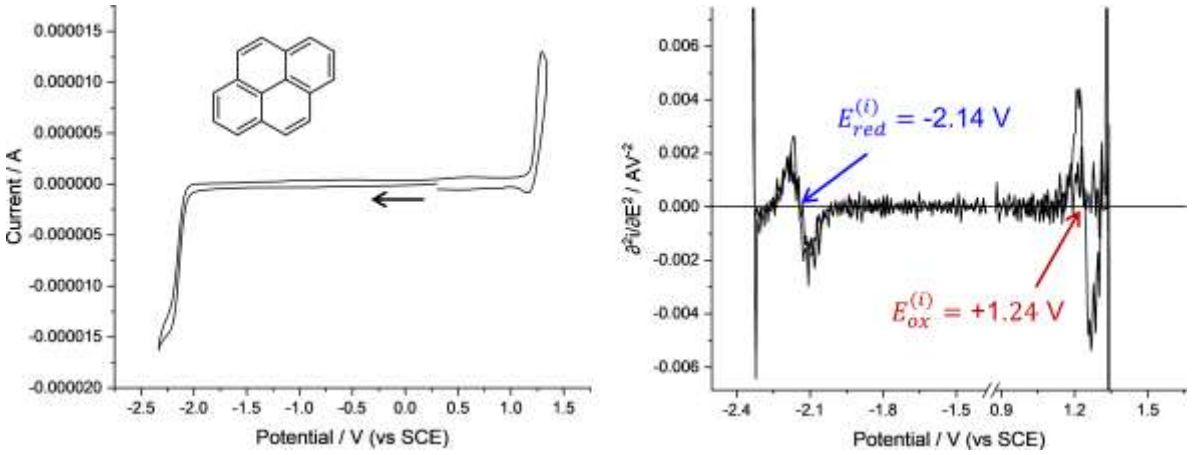

Figure S5. Cyclic voltammetry of Pyrene (**P**) on a glassy carbon electrode in acetonitrile + 0.1 mol L^{-1} of (nBu_4N)[PF_6])at 0.1 V s^{-1} (left); redox potentials at the inflection points are indicated on the corresponding second derivative plot (right).

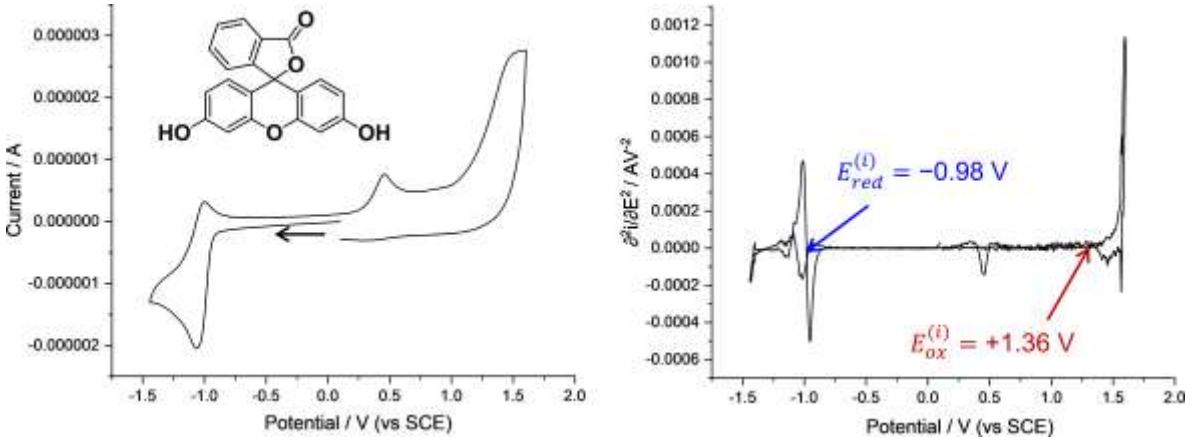

Figure S6. Cyclic voltammetry of fluorescein on a glassy carbon electrode in acetonitrile + 0.1 mol L^{-1} of (nBu_4N)[PF_6])at 0.1 V s^{-1} (left); redox potentials at the inflection points are indicated on the corresponding second derivative plot (right). The recorded voltammogram is not consistent with the indicated structure of fluorescein (**FL**), and may correspond to the dianionic form of fluorescein. [3]

S3. DFT Computations

Optimized geometries were computed within the framework of the Density Functional Theory using the *Gaussian* 16 software package. [4] The optimizations were carried out using the M06-2X functional combined with the double-ζ 6-31+G(d,p) basis set, to take into account non-covalent interactions, for which meta-GGA functionals usually outperform many other hybrid functionals. [5] Calculations were carried out in vacuum and in solution. Unless specified, solvent effects were taken into account implicitly under the Polarizable Continuum Model (PCM). The vibrational spectra for the optimized geometries were systematically inspected to possess zero imaginary frequencies in the case of energy minima, to confirm them as true stationary states. Conversely, in the case of transition state **TS1** in methanol a single imaginary frequency corresponding to the scanned reaction coordinate was found, at ν = -962.74 cm^{-1}. Comparisons between experimental and computed vibrational frequencies, considered a 0.952 scaling factor on DFT data. [6]

In the case of conformationally flexible molecules or (e.g. **FO**), no significant efforts were carried out to find their global energy minima as only insignificant electronic differences are expected among their various conformers. Contrarywise, several different starting conformations were tested for **DEHP** and for supramolecular adducts, due to the relevance of their conformation in the present study. It should be noted that although rarely acknowledged, **DEHP** is a chiral molecule which is commercialized as a mixture of its equally-abundant R/R, R/S and S/S diastereomers. [7] Anticipating largely invariant electronic properties for the three diastereomers, the DFT computations were arbitrarily carried out on the R/S diastereomer. In an attempt to find a conformation for **DEHP** as close as possible to its global minimum, the potential energy surface (PES) of this phthalate was scanned along the rotation of the two ester groups using the semiempirical PM6 method in vacuum, using a 10 deg step size. The molecular structure was allowed to relax freely at every step of the scan. The minimum energy conformation found in the resulting 2D PES scan (Figure S7) was used as input for a full DFT optimization as described above.

TD-DFT computations were carried out on optimized geometries in solution to assist optical spectrum assignments. Excitations to the 20 lowest-lying excited states were systematically included to gain a good description for high energy optical absorption bands. As shown in Figures S8-13, a good agreement between the experimental spectra and the DFT-predicted excitations was found, with a tendency towards slightly higher calculated energies, which is common for DFT. [8] In order to confirm or correct the NMR assignments for the various tautomers of fluorescein, Gaussian Invariant Atomic Orbital (GIAO) computations of the isotropic magnetic shieldings of ^{13}C nuclei were performed at the same level of theory. Although the methodology employed provides absolute chemical shifts, for comparison the calculated values were scaled with respect to an external tetramethylsilane (TMS) reference computed at the B3LYP/6-311+G(2d,p) level of theory.

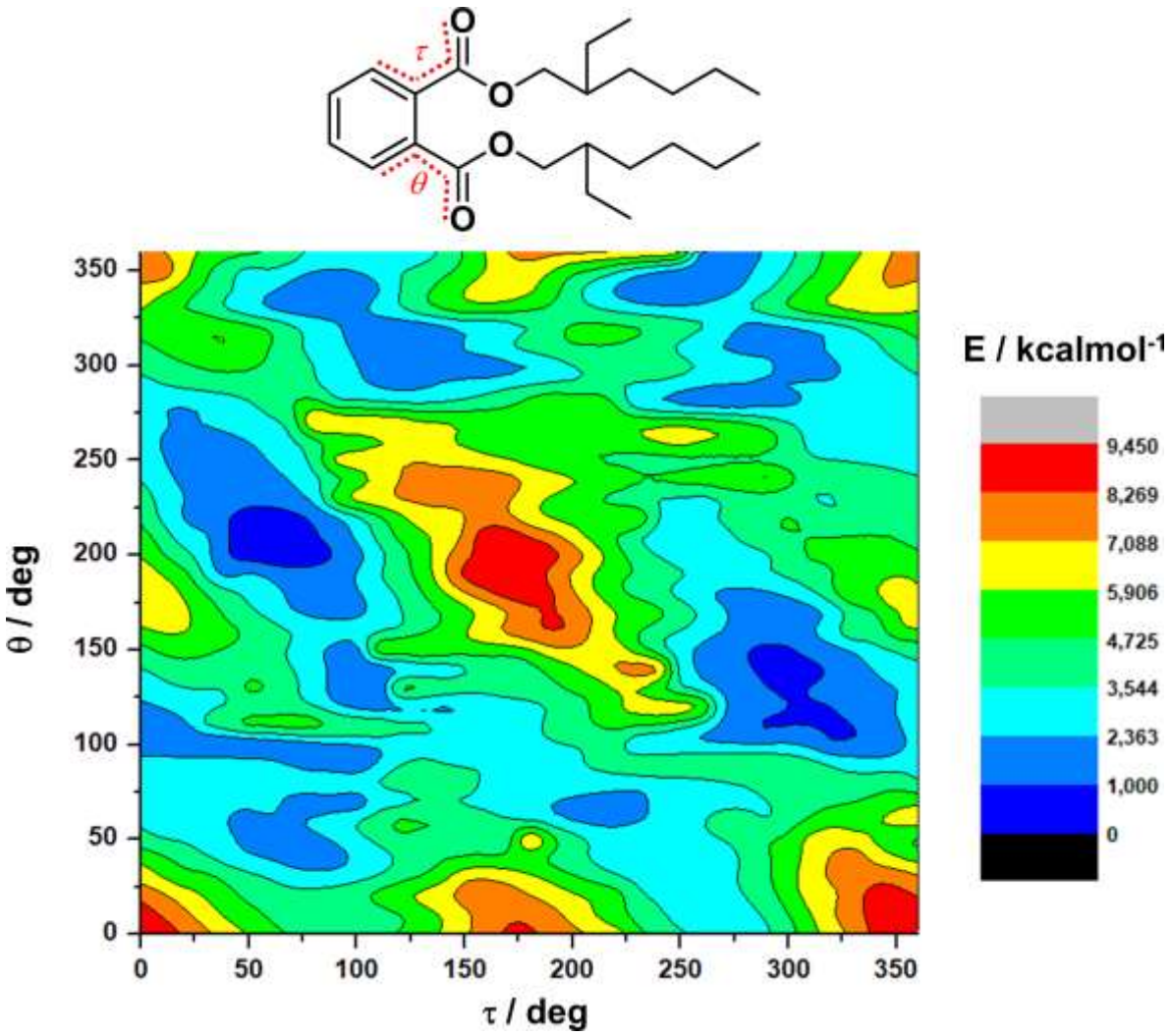

Figure S7. Relaxed 2D potential energy surface (PES) scan for di(2-ethylhexyl) phthalate (**DEHP**) at the PM6 level in vacuum, with a 10-degree step size.

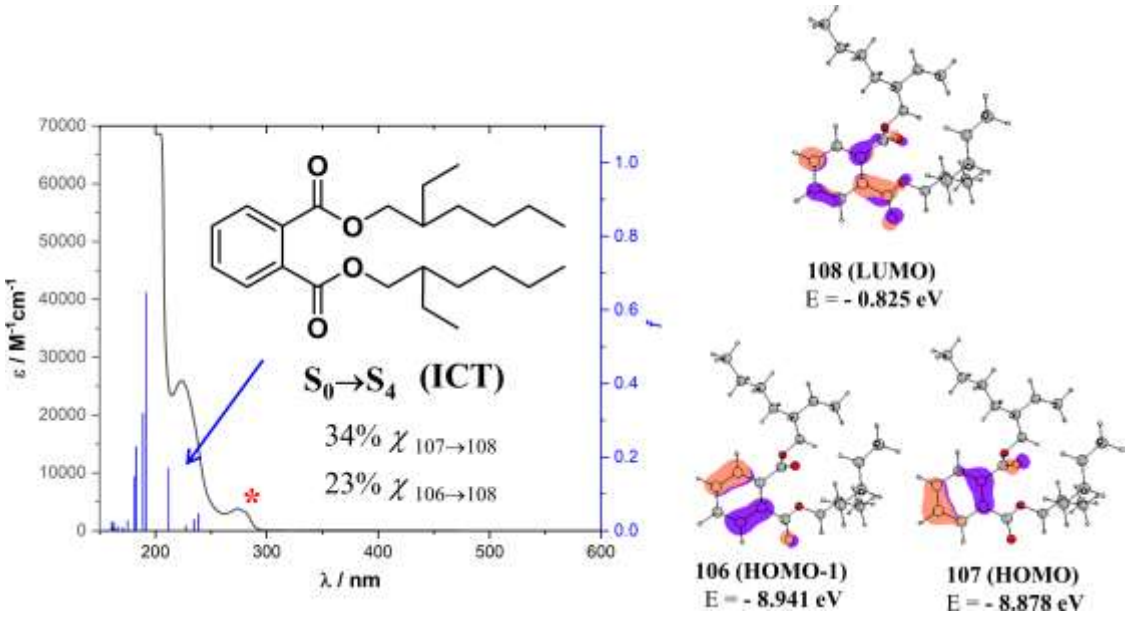

Figure S8. Comparison of the experimental optical absorption spectrum (black line) and the DFT-computed excitations (blue lines, M06-2X/6-31+G**/PCM) in acetonitrile for di(2-ethylhexyl) phthalate (**DEHP**). Assignments for the lowest-lying band are indicated as well as the main electronic transition and a representation and energy of the involved molecular orbitals. Symmetry-forbidden or vibronic bands were not taken into consideration in the DFT computation and are signaled with asterisks.

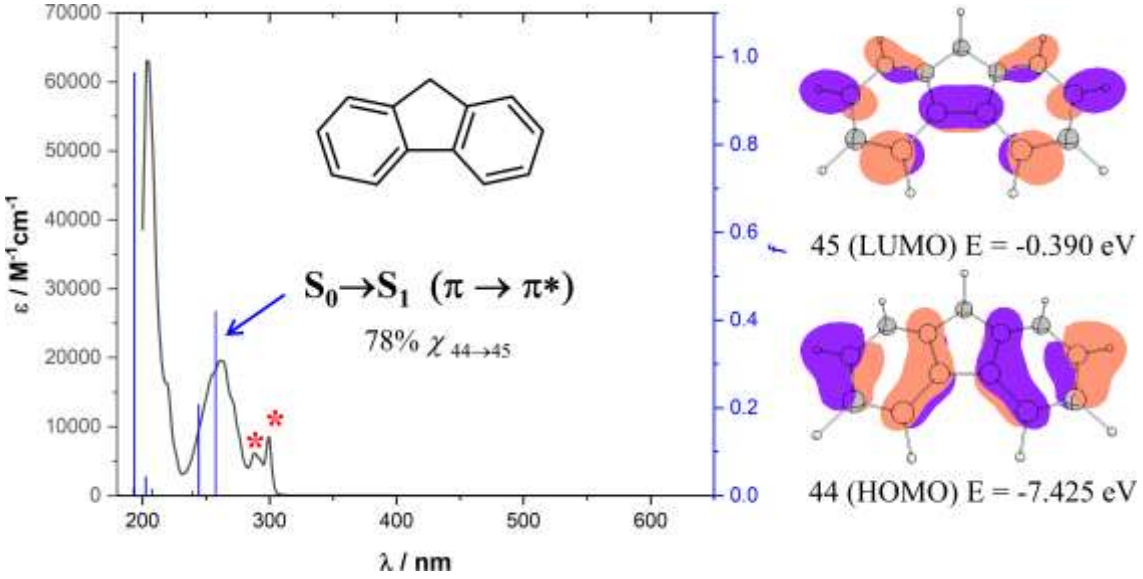

Figure S9. Comparison of the experimental optical absorption spectrum (black line) and the DFT-computed excitations (blue lines, M06-2X/6-31+G**/PCM) in acetonitrile for 9*H*-fluorene (**F**). Assignments for the lowest-lying band are indicated as well as the main electronic transition and a representation and energy of the involved molecular orbitals. Symmetry-forbidden or vibronic bands were not taken into consideration in the DFT computation and are signaled with asterisks.

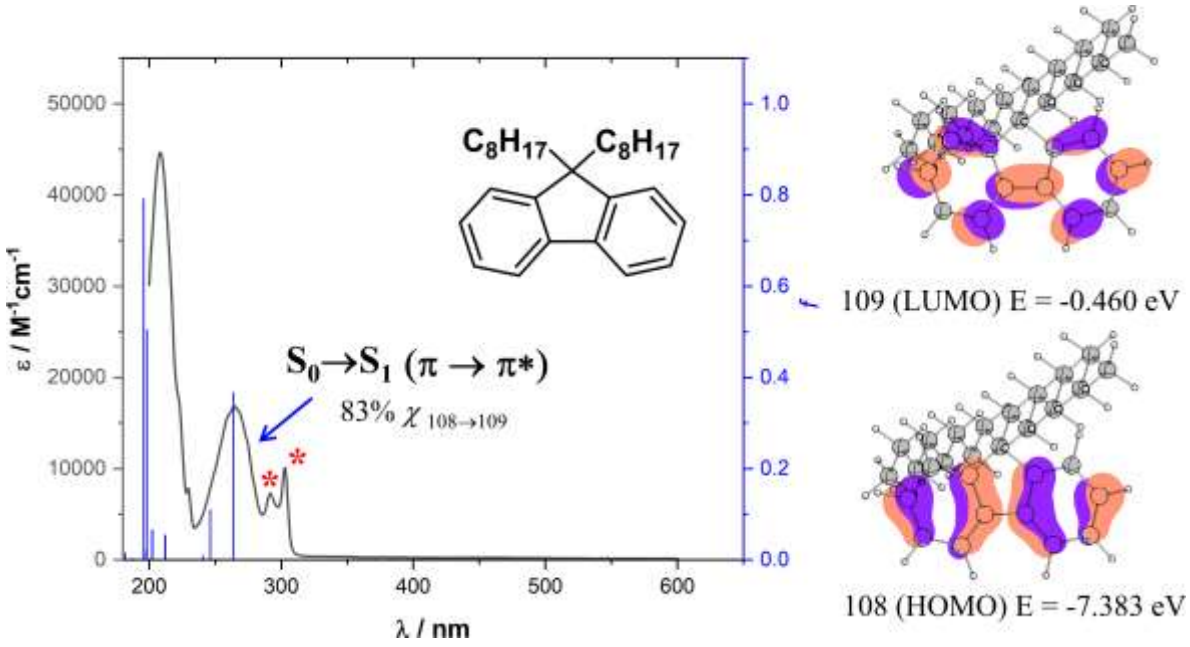

Figure S10. Comparison of the experimental optical absorption spectrum (black line) and the DFT-computed excitations (blue lines, M06-2X/6-31+G**/PCM) in acetonitrile for 9,9-dioctylfluorene (**FO**). Assignments for the lowest-lying band are indicated as well as the main electronic transition and a representation and energy of the involved molecular orbitals. Symmetry-forbidden or vibronic bands were not taken into consideration in the DFT computation and are signaled with asterisks.

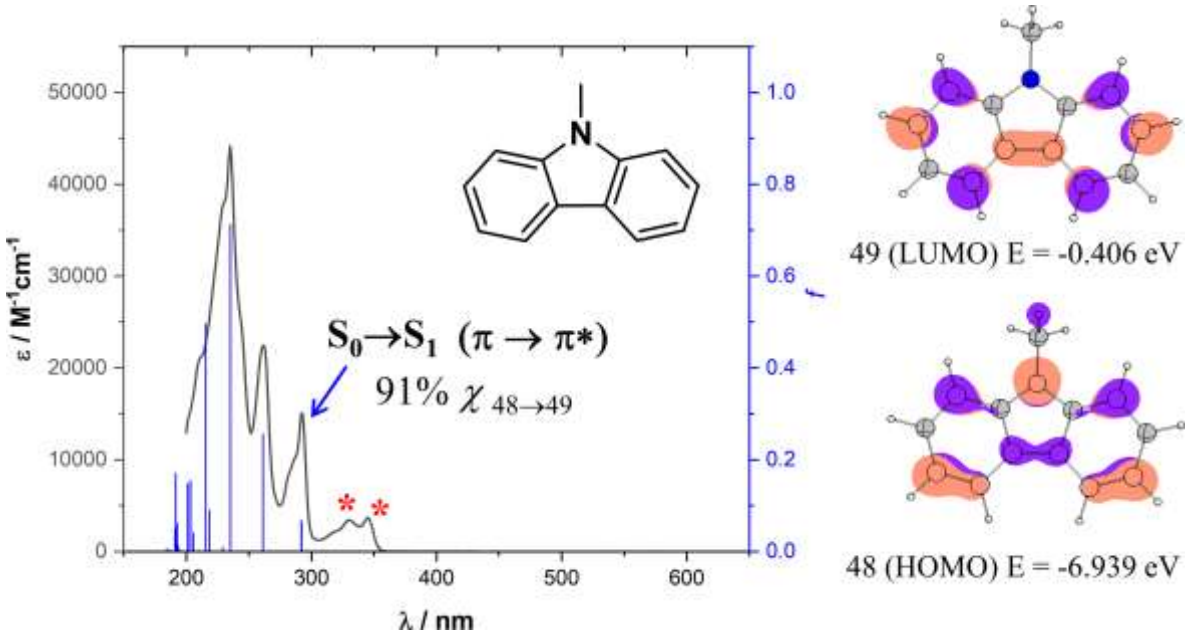

Figure S11. Comparison of the experimental optical absorption spectrum (black line) and the DFT-computed excitations (blue lines, M06-2X/6-31+G**/PCM) in acetonitrile for 9-methylcarbazol (**C**). Assignments for the lowest-lying band are indicated as well as the main electronic transition and a representation and energy of the involved molecular orbitals. Symmetry-forbidden or vibronic bands were not taken into consideration in the DFT computation and are signaled with asterisks.

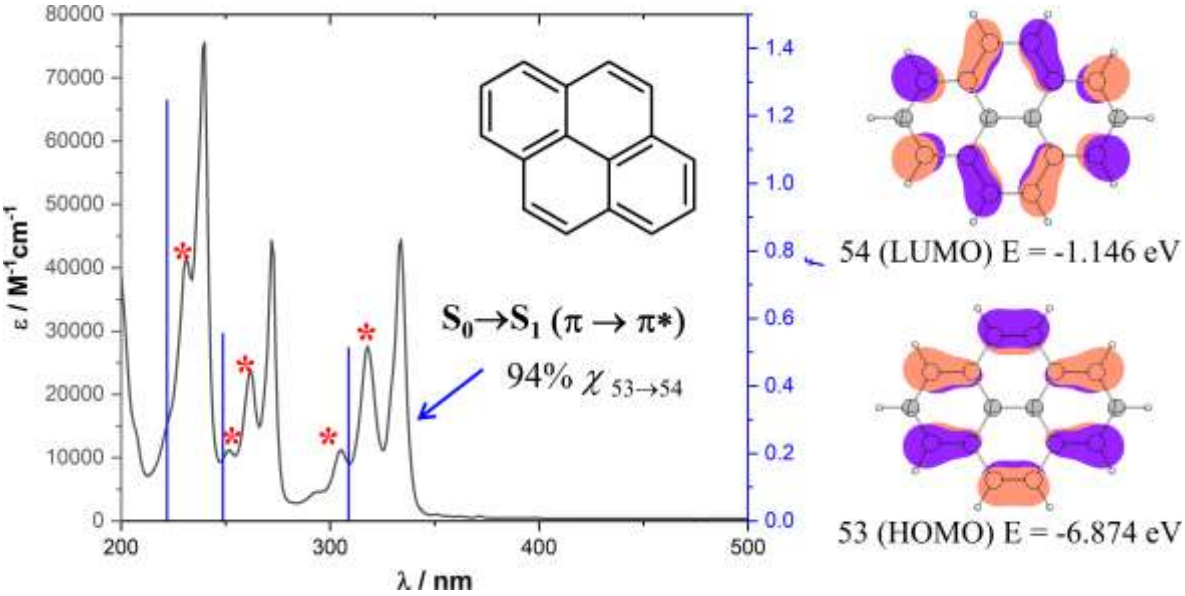

Figure S12. Comparison of the experimental optical absorption spectrum (black line) and the DFT-computed excitations (blue lines, M06-2X/6-31+G**/PCM) in acetonitrile for pyrene (**P**). Assignments for the lowest-lying band are indicated as well as the main electronic transition and a representation and energy of the involved molecular orbitals. Symmetry-forbidden or vibronic bands were not taken into consideration in the DFT computation and are signaled with asterisks.

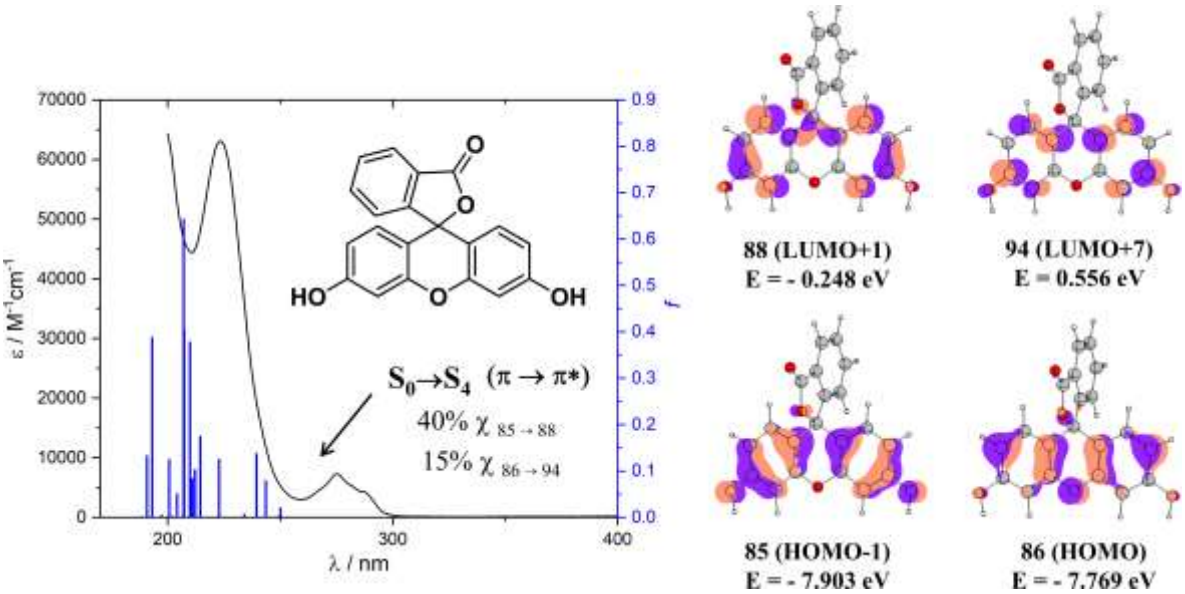

Figure S13. Comparison of the experimental optical absorption spectrum (black line) and the DFT-computed excitations (blue lines, M06-2X/6-31+G**/PCM) in acetonitrile for the lactoid tautomer of fluorescein (**FL**). The experimental spectrum was recorded from a freshly prepared analytical sample of the compound as an acetone solvate (**FL-Me$_2$CO**). Assignments for the lowest-lying band are indicated as well as the main electronic transition and a representation and energy of the involved molecular orbitals.

DFT computations were also carried out on **DEHP**/fluorophore adducts to investigate their conformation and interaction energies. It should be noted that the objective was not to identify the global minimum for each adduct, which is beyond the scope of this paper given the significant flexibility of the alkyl chains of **DEHP**. Instead, the objective was to identify stable adducts that exhibited a π-stacking interaction between the two molecules, as this would result in the greatest orbital overlap. A preliminary investigation was conducted to identify the most promising initial conformations. This was achieved by initially examining a smaller phthalate, namely dimethyl phthalate (**DMP**). Following optimization, the lowest-energy conformer identified among the **DMP**-fluorophore adducts was employed to construct a comprehensive model of the adduct with **DEHP**. These computations were conducted in both acetonitrile and in vacuum to assess the potential influence of the solvent on the stability of these conformations, which is a crucial consideration given that the experimental detection of **DEHP** in this manuscript was not performed in solution.

As a result of the computational investigation described above, stable conformations were successfully identified for all the adducts. The results are presented in Table S1 and illustrated in Figures S14-S15. As can be observed, the aggregates exhibit π-stacking interactions with relatively short intermolecular distances, as evidenced by the shortest intercentroid distances (d_i). The fluorophores and **DEHP** are held together by moderate to strong interaction energies (E_{int}), which are determined as the potential energy difference between the adduct and the sum of the individual fragments. Furthermore, a discernible orbital overlap is evident between the highest occupied molecular orbital (HOMO) situated at the fluorophore and the lowest unoccupied molecular orbital (LUMO) located at **DEHP**. This observation aligns with the potential for electron transfer from the fluorophores to **DEHP** upon the formation of these supramolecular aggregates. Two exceptions require further elucidation. The first is the **P-DEHP** adduct, which exhibited both the LUMO and HOMO within the fluorophore. Nevertheless, the LUMO of **DEHP** was found to lie below that of **P** via electrochemical methods, rendering this exception an artifact. On the other hand, the **FL-DEHP** adduct exhibited a LUMO situated in both **DEHP** and the benzofuran fragment in **FL**, which may indicate the potential for a competing intramolecular PET process within **FL**. A comprehensive investigation would be necessary to definitively exclude this possibility. However, the orthogonal orientation between the benzofuranone and xanthene fragments of this fluorophore suggests that orbital overlap is likely to be minimal, thereby impeding the potential competing intramolecular PET process. In any case, the computations demonstrated that **DEHP** and the various fluorophores can establish moderate to strong π-interactions with notable orbital overlap. Furthermore, the solvent does not appear to play a significant role in stabilizing these adducts, as analogous results were consistently obtained in vacuum and acetonitrile.

Table S1. DFT-computed minimum intercentroid distance (d_i) and interaction energy (E_{int}) for supramolecular adducts between **DEHP** and the fluorophores at the M06-2X/6-31+G(d,p)/PCM level of theory.

	d_i / Å		E_{int} / kJmol^{-1}	
	Vacuum	Acetonitrile	Vacuum	Acetonitrile
FL-DEHP	3.67	3.67	-64.57	-56.74
F-DEHP	3.51	3.51	-43.53	-40.06
FO-DEHP	4.02	4.02	-47.51	-52.02
C-DEHP	3.40	3.42	-50.70	-46.93
P-DEHP	3.53	3.53	-55.75	-50.78

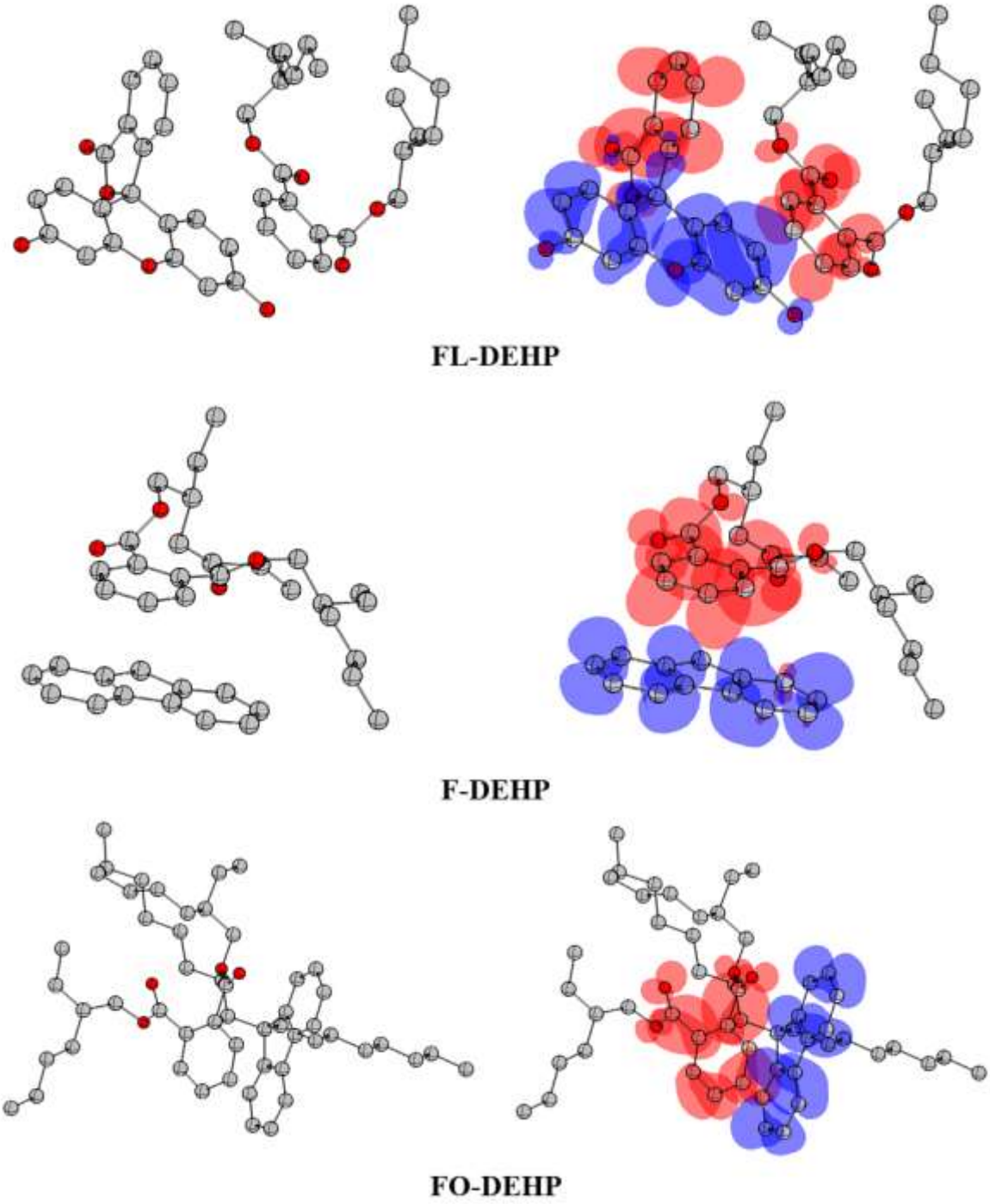

Figure S14. DFT-optimized molecular structure (left) and representation of the frontier molecular orbitals (right, HOMO: blue, LUMO: red) for adducts **FL-DEHP**, **F-DEHP** and **FO-DEHP** at the M06-2X/6-31+G** level in acetonitrile (H-atoms omitted for clarity).

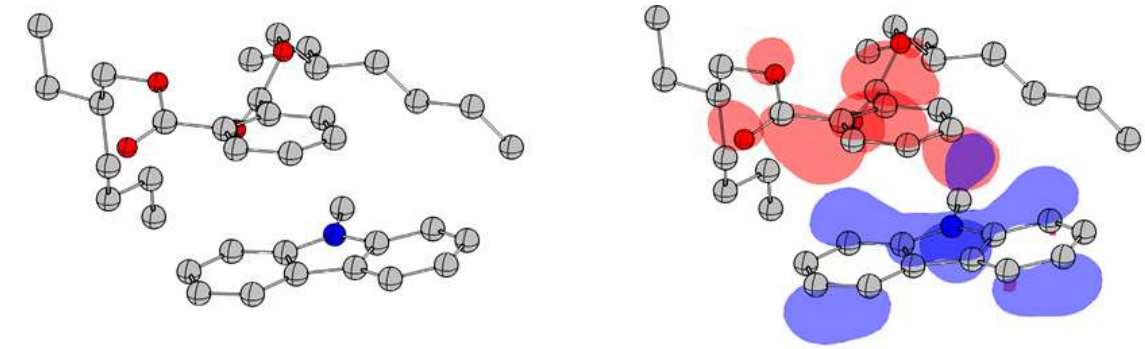

C-DEHP

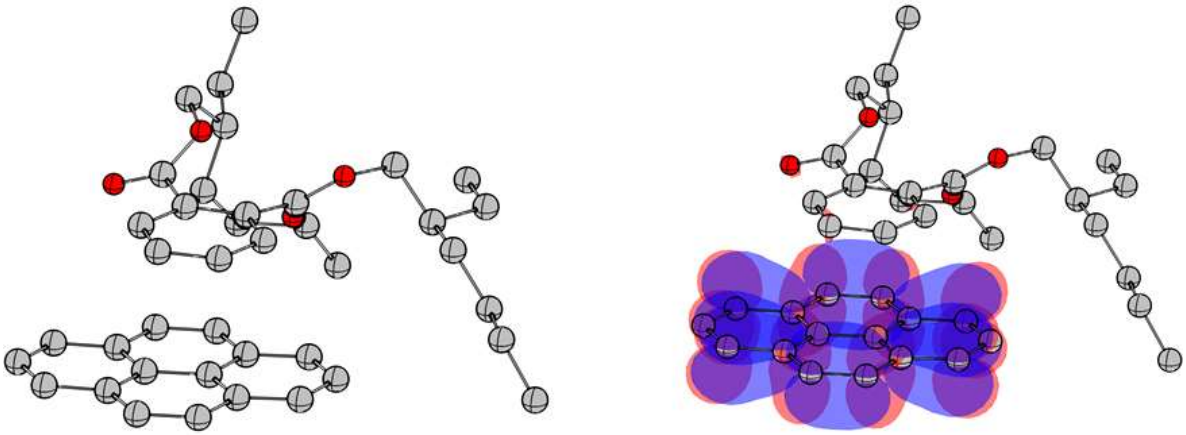

P-DEHP

Figure S15. DFT-optimized molecular structure (left) and representation of the frontier molecular orbitals (right, HOMO: blue, LUMO: red) for adducts **C-DEHP** and **P-DEHP** at the M06-2X/6-31+G** level in acetonitrile (H-atoms omitted for clarity).

S4. Photophysical Characterization

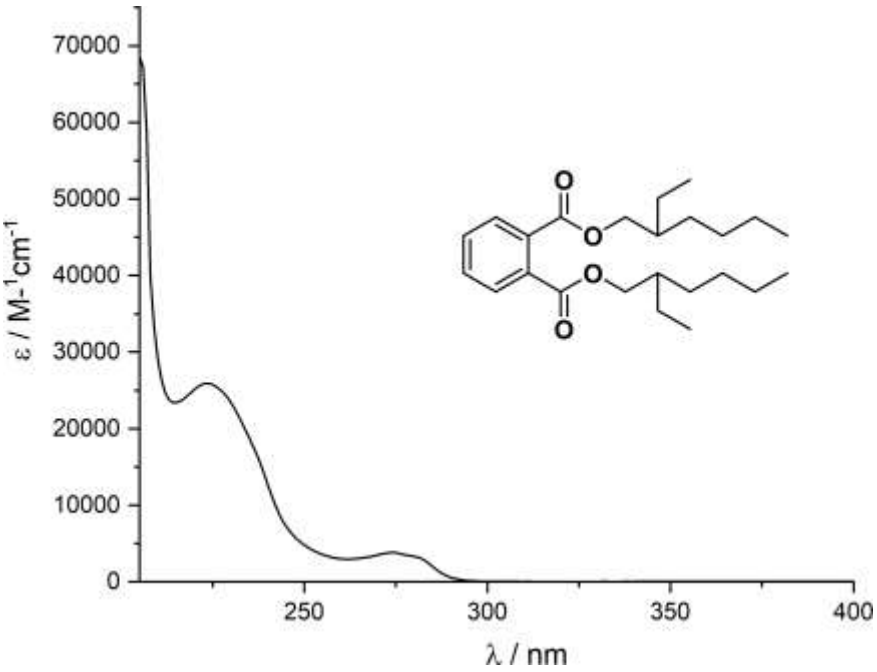

Figure S16. UV-visible absorption spectrum for di(2-ethylhexyl) phthalate (**DEHP**) in acetonitrile.

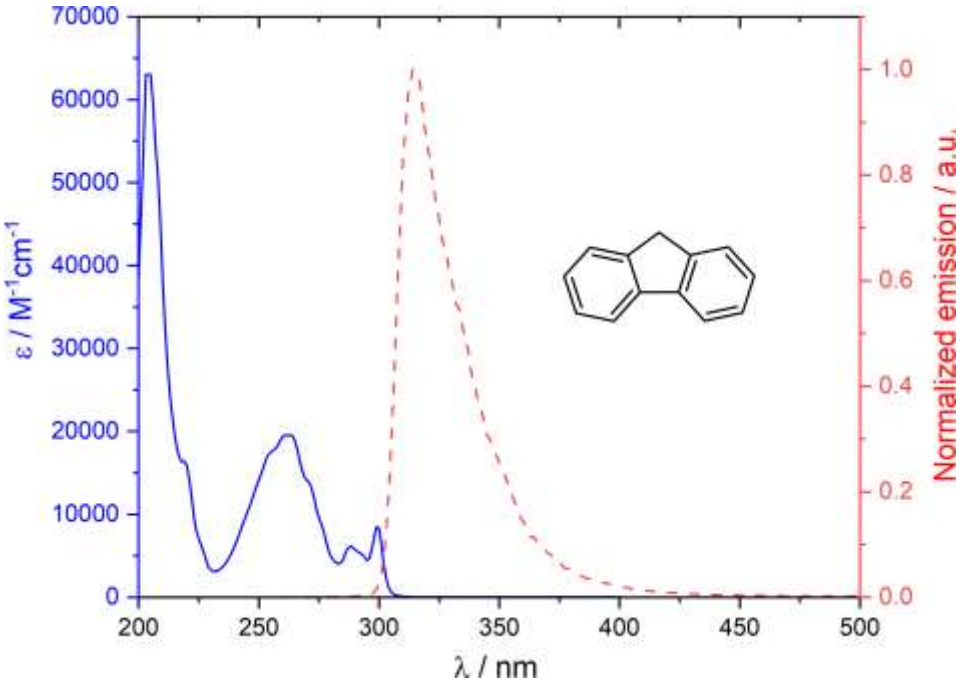

Figure S17. UV-visible absorption and fluorescence (λ_{exc} = 240 nm) spectra for 9*H*-fluorene (**F**) in acetonitrile.

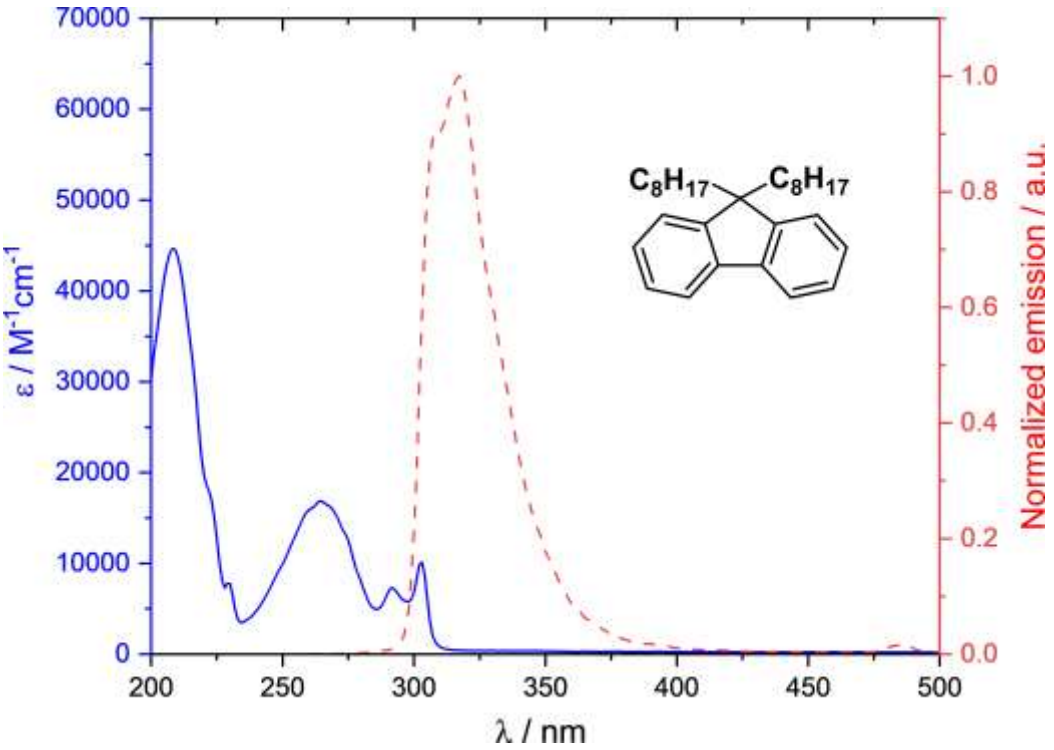

Figure S18. UV-visible absorption and fluorescence (λ_{exc} = 240 nm) spectra for 9,9-dioctylfluorene (**FO**) in acetonitrile.

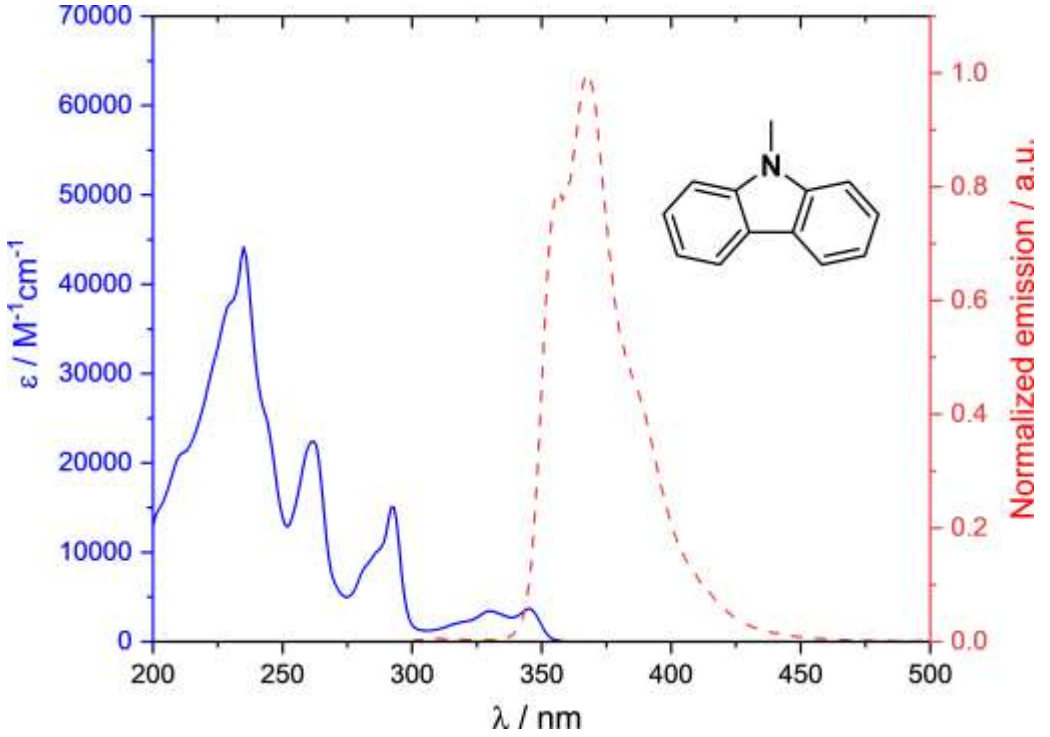

Figure S19. UV-visible absorption and fluorescence (λ_{exc} = 240 nm) spectra for 9-methylcarbazol (**C**) in acetonitrile.

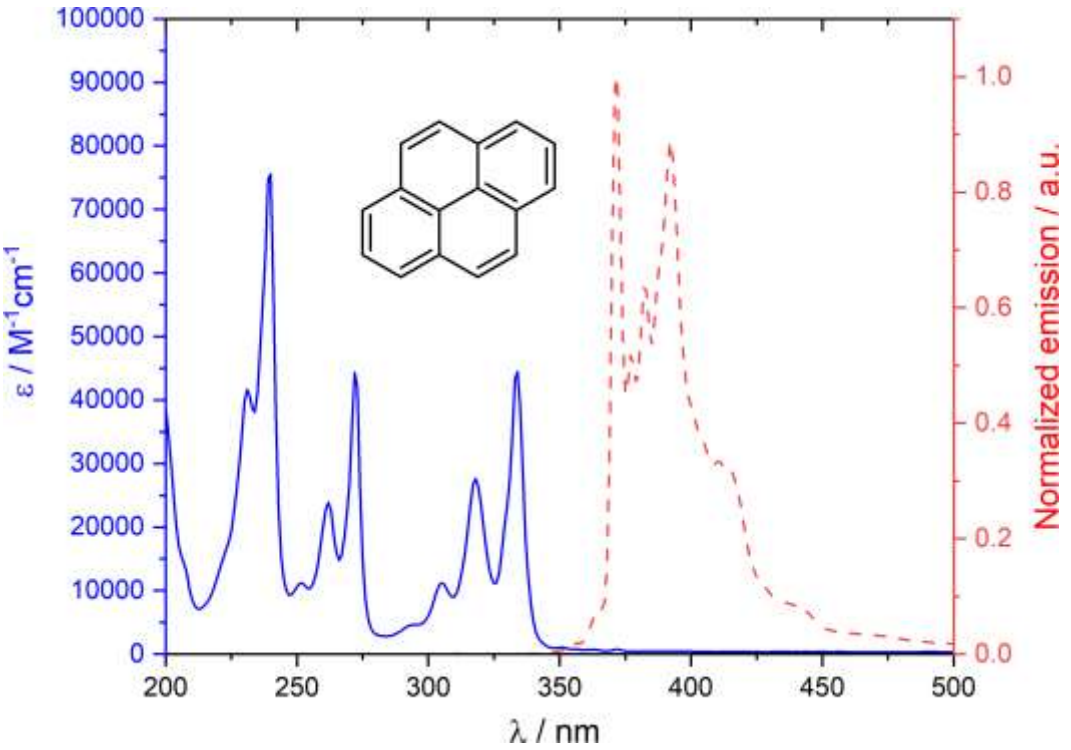

Figure S20. UV-visible absorption and fluorescence (λ_{exc} = 285 nm) spectra for pyrene (**P**) in acetonitrile.

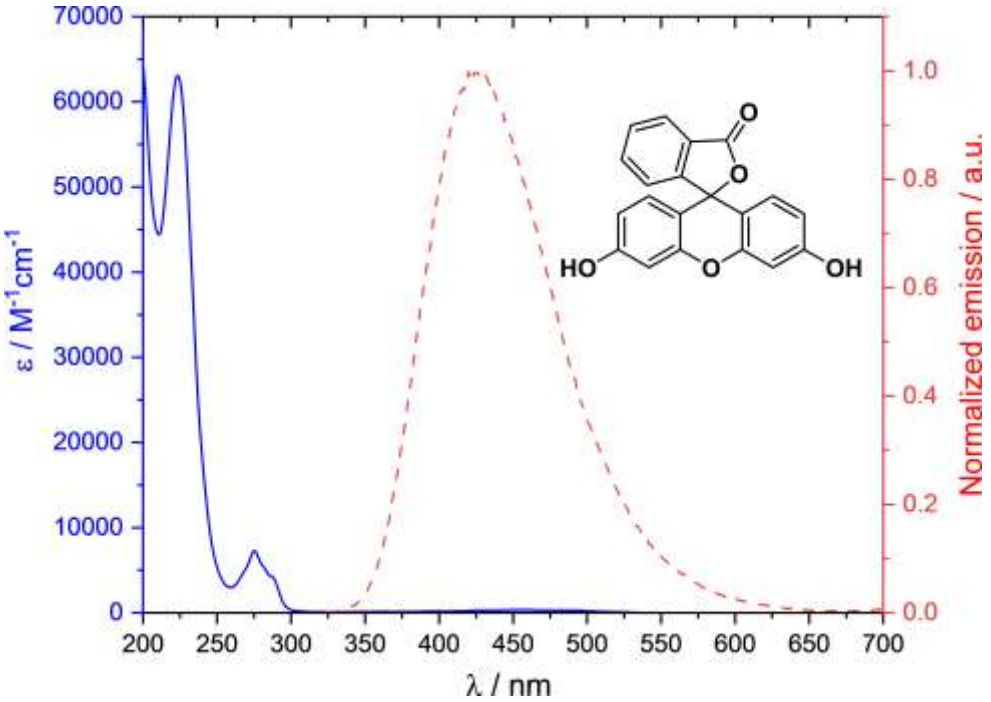

Figure S21. UV-visible absorption and fluorescence (λ_{exc} = 285 nm) spectra for the lactoid tautomer of fluorescein (**FL**) in acetonitrile. The spectra were recorded from a freshly prepared analytical sample of the compound as an acetone solvate (**FL-Me_2CO**).

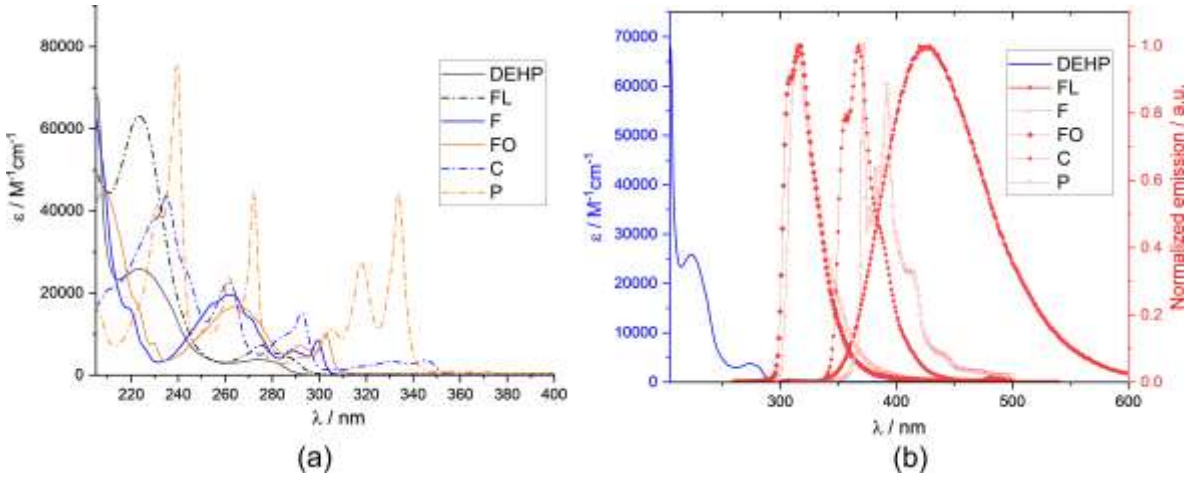

Figure S22. Overlay of the optical absorption spectra of **DEHP** with (a) the optical absorption and (b) the fluorescence spectra of the different fluorophores under investigation. Measurements were performed in acetonitrile at 298 K. Emission spectra were measured after excitation at λ = 240 nm (**F**, **FO**, **C**) or λ = 285 nm (**P**, **FL**). Spectra for **FL** were recorded from a freshly prepared analytical sample of the compound as an acetone solvate (**FL-Me_2CO**).

S5. Filter Paper Tests

Test filter papers were prepared according to the following methodology, which is based on previous reports on TNT detection with modifications. [9] For each fluorophore, 10 Whatman #41 ashless 47 mm filter papers were weighed and introduced inside a crystallizer containing a $5{,}0x10^{-5}$ M solution of the fluorophore in acetone (**F**, **FO**, **P**, **C**) or methanol (**FL**), the crystallizer was closed and the solution was absorbed in the test papers for 20 s. The papers were then dried for 3 h at 50 °C inside an oven and weighed. From the weigh differences and considering the area of the papers, the surface concentration of the absorbed fluorophores was found in the range between $4.61x10^{-5}$ to $6.98x10^{-5}$ gcm^{-2}. The tests with **DEHP** solutions were carried by triplicate by placing 5 μL of **DEHP** solutions in pentane at varying concentrations on different spot on a single filter paper. The papers were allowed to air-dry and then the fluorescence at each spot was measured in using the optical setup shown in Figure S23. Tests with **DEHP** vapors were carried out at room temperature by placing a test paper inside a glass desiccator containing liquid **DEHP**. The desiccator was then connected to a Schlenk line and vacuum was applied. After reaching a 0.95 mbar pressure, a clear bubbling of the **DEHP** inside the desiccator was observed. The desiccator was then closed for 13 days. The fluorescence of the papers was finally measured and compared to a paper that was not exposed to the **DEHP** vapors.

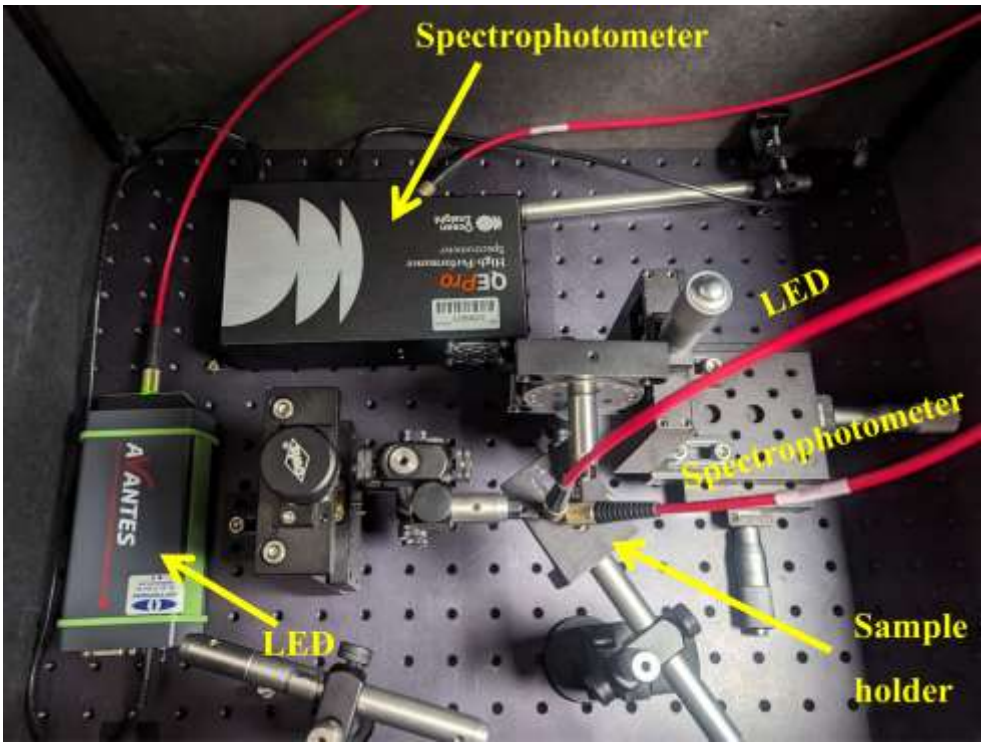

Figure S23. Optical setup employed for the steady-state fluorescence measurements on test filter papers, consisting of a black box containing an adjustable sample holder where the test paper is placed. The material is then illuminated by a LED of a suitable wavelength and aimed by a fiber optic-based high sensitivity spectrophotometer. The box is then closed and the optical spectrum recorded.

S6. Synthesis and Characterization of Fluorescein Solvates

The synthesis of the different solvates of the lactoid tautomer of fluorescein (**FL**) was carried out as depicted in Scheme S1, following the informed synthesis of the acetone solvate (**FL-Me$_2$CO**)[10] with some modifications. The products were obtained by dissolving the commercial, red, quinoid tautomer of fluorescein (**FQ**) in the minimum amount of a given solvent. In the case of the acetone solvate, once fully dissolved, the sample was consequently concentrated under reduced pressure before the next step. The saturated solutions were then precipitated by dropping in an excess of *n*-hexane or of a mixture of *n*-hexane and chloroform, using the minimum amount of chloroform necessary to obtain a homogeneous mixture of the three solvents. This led to the target solvates as pale-yellow precipitates that were collected, washed with *n*-hexane and dried. The identity of the solvates, obtained as yellow solids, was corroborated by IR spectroscopy, where the assignment of the characteristic bands of the fluorophore and the various solvents was performed with support from DFT computations (Supplementary Figures S24-S26). The solvates were also characterized by elemental and thermogravimetric analyses, showing that these materials were obtained as 1/1 solvates in the case of **FL-Me$_2$CO** and **FL-DMF**, whereas the **FL-DMSO** solvate contained nearly three molecules of solvent per molecule of fluorescein, which are released at T = 134 to 167 °C with a concomitant color change to red (Supplementary Figure S27).

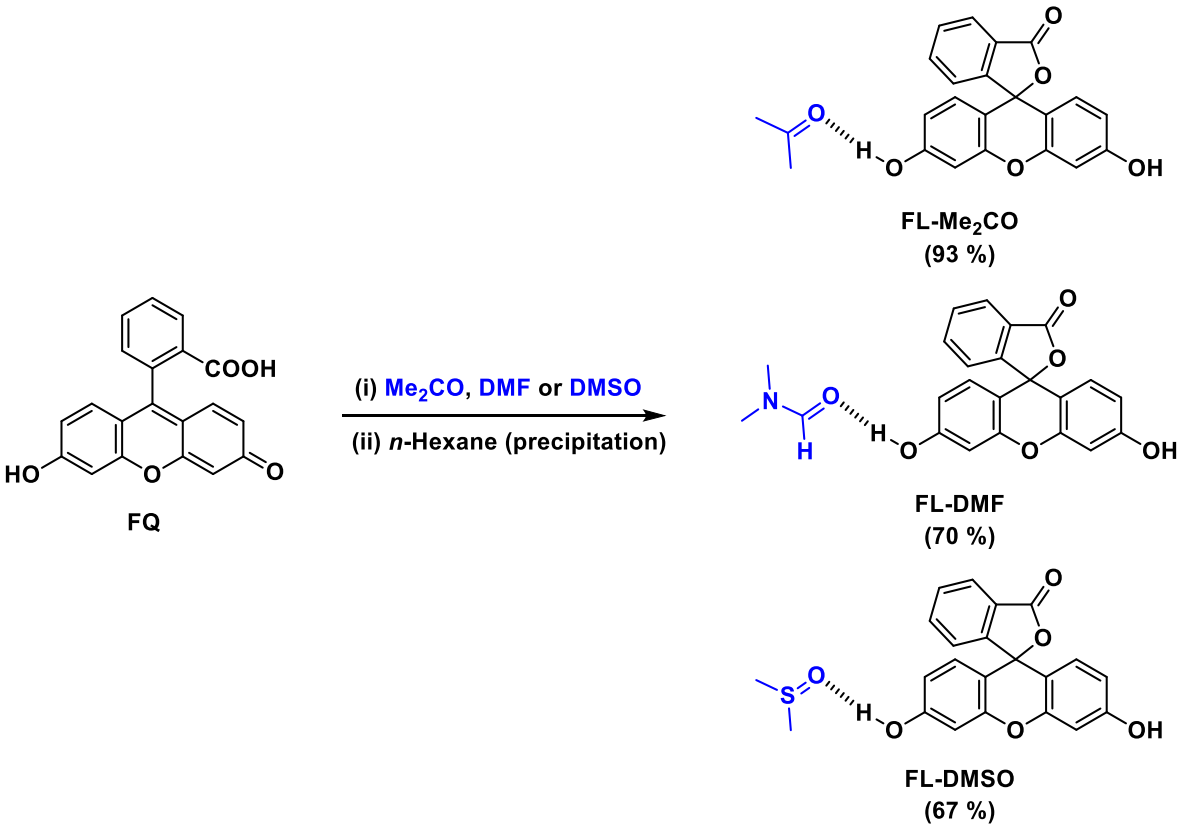

Scheme S1. Synthesis of the different solvates of the lactoid tautomer of fluorescein. Potential hydrogen-bonded structures for 1/1 solvates are shown only for indicative purposes. It should be noted that, as detailed below, the **FL-DMSO** solvate was obtained as a 1/3 solvate.

FL-Me_2CO. To a beaker containing fluorescein (**FQ**) (1.00 g, 3.0 mmol) was added acetone (300 mL) with stirring and the solution was concentrated *in vacuo* to ca. 10 mL. The solution was then filtered through cotton to remove undissolved material and dropped slowly on *n*-hexane (600 mL). The precipitate thus obtained was collected, washed with *n*-hexane and dried *in vacuo* to yield 1.09 g (2.8 mmol, 93 %) of the **FL-Me_2CO** (1/1) solvate as a clear yellow solid. **FT-IR** (ATR, cm^{-1}) 3317 (νO-H, H-bonded to C=O), 1721 (νC=O, FL), 1699 (νC=O, acetone). **Elemental analysis** found: C, 70.60; H, 3.95. Required for $C_{20}H_{12}O_5$ (C_3H_6O): C, 70.76; H, 4.65.

FL-DMF. To a beaker containing fluorescein (**FQ**) (1.00 g, 3.0 mmol) was added dimethylformamide (1.0 mL) and chloroform (10 mL). This solution was added slowly with mechanical stirring to a beaker containing *n*-hexane (700 mL), leading to the slow formation of a precipitate under stirring. The solid thus obtained was collected, washed with *n*-hexane and dried in vacuo to yield 0.85 g (2.1 mmol, 70 %) of the **FL-DMF** (1/1) solvate as a clear yellow solid. **FT-IR** (ATR, cm^{-1}) 3414 (νO-H, H-bonded to C=O), 1719 (νC=O, FL), 1658 (νC=O, dimethylformamide). **Elemental analysis** found: C, 67.38; H, 4.58; N, 3.49. Required for $C_{20}H_{12}O_5$ (C_4H_7NO): C, 68.14; H, 4.72; N, 3.46.

FL-DMSO. To a beaker containing fluorescein (**FQ**) (1.00 g, 3.0 mmol) was added dimethylsulfoxide (2.5 mL) and chloroform (40 mL). This solution was added slowly with mechanical stirring to a beaker containing *n*-hexane (700 mL), leading to the slow formation of a precipitate under stirring. The solid thus obtained was collected, washed with *n*-hexane and dried in vacuo to yield 1.11 g (2.0 mmol, 67 %) of the **FL-DMSO** (1/3) solvate as a clear yellow solid. **FT-IR** (ATR, cm^{-1}) 3420 (νO-H, H-bonded to C=O), 1724 (νC=O, FL), 1012 (νS=O). **Elemental analysis** found: C, 54.33; H, 4.59. Required for $C_{20}H_{12}O_5$ ($3xC_3H_6OS$, $1.85xH_2O$): C, 54.76; H, 5.34.

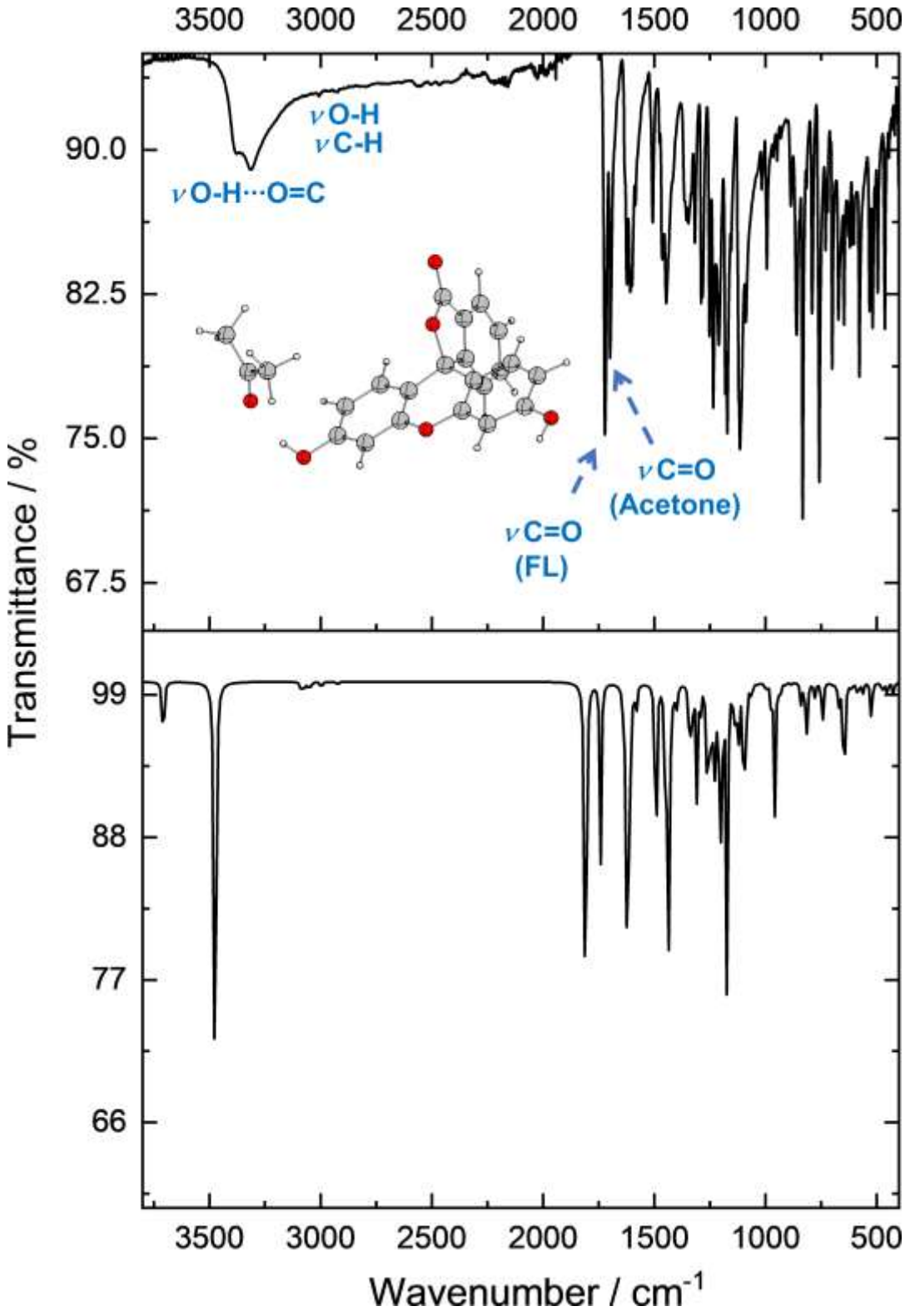

Figure S24. Experimental (FTIR-ATR, top) and DFT-computed (M06-2X/6-31+G** in vacuum, bottom) IR spectra for the acetone solvate of the lactoid tautomer of fluorescein (**FL-Me$_2$CO**). DFT-computed frequencies were scaled by 0.952. [6]

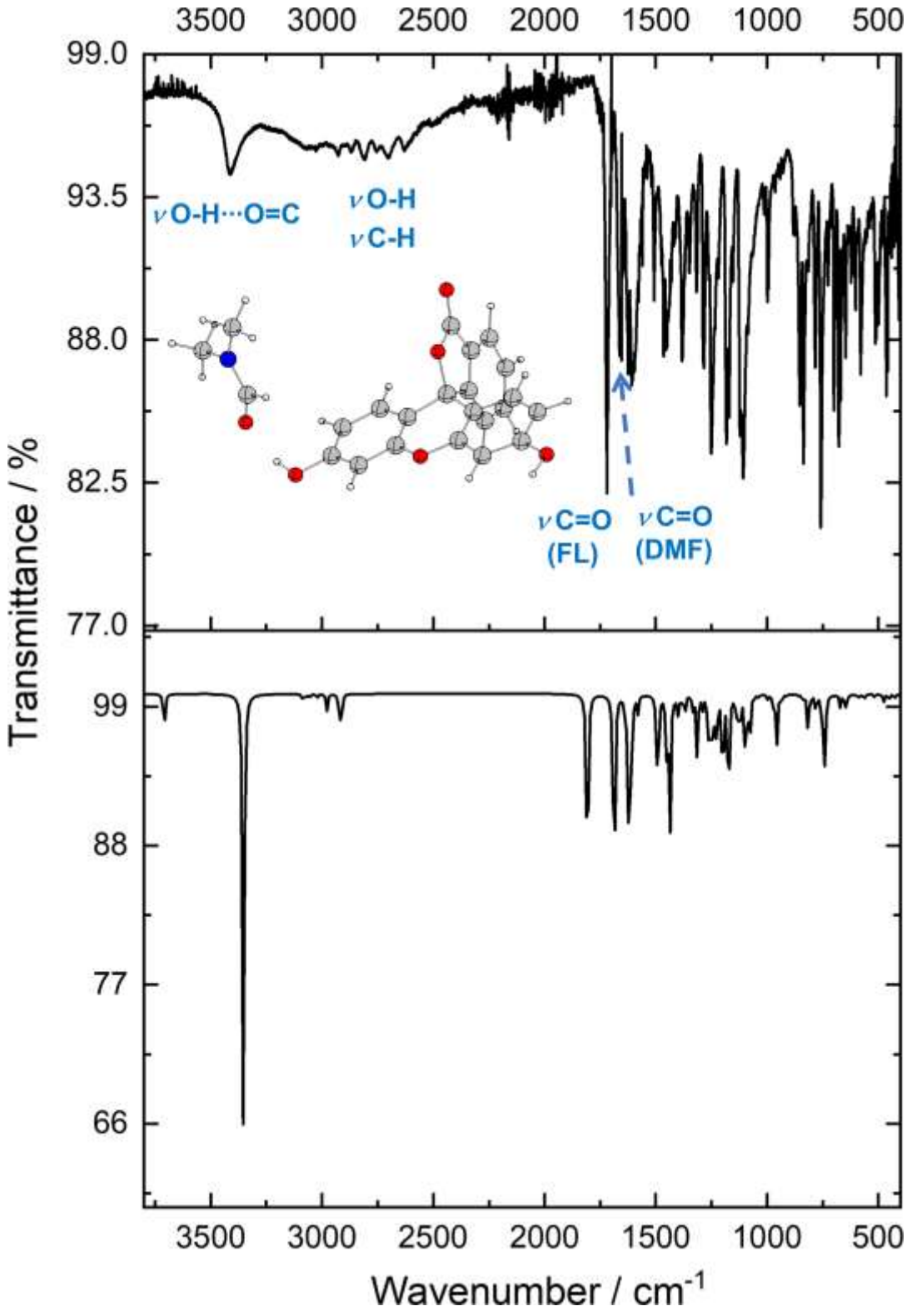

Figure S25. Experimental (FTIR-ATR, top) and DFT-computed (M06-2X/6-31+G** in vacuum, bottom) IR spectra for the dimethylformamide solvate of the lactoid tautomer of fluorescein (**FL-DMF**). DFT-computed frequencies were scaled by 0.952. [6]

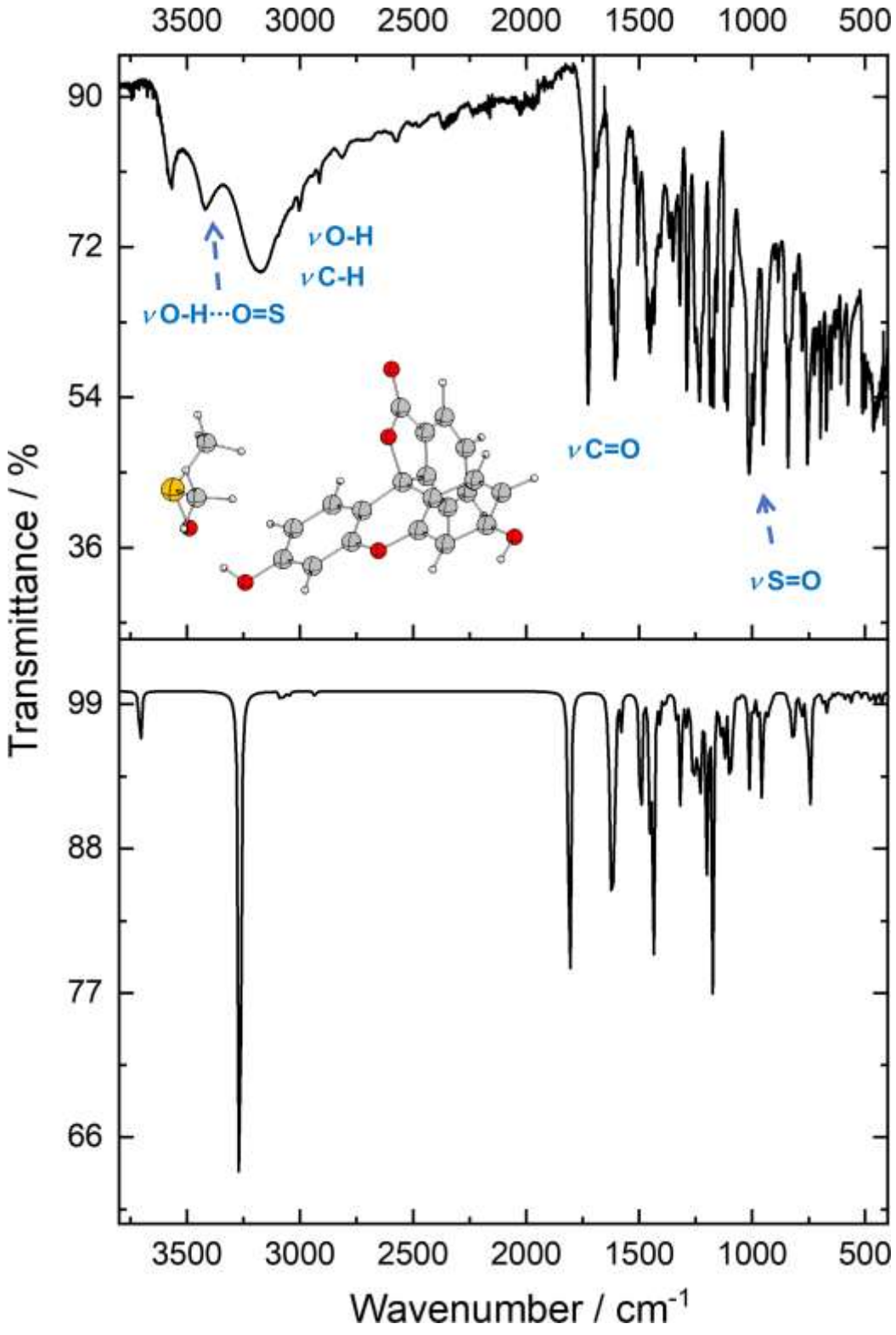

Figure S26. Experimental (FTIR-ATR, top) and DFT-computed (M06-2X/6-31+G** in vacuum, bottom) IR spectra for the dimethylsulfoxide solvate of the lactoid tautomer of fluorescein (**FL-DMSO**). DFT-computed frequencies were scaled by 0.952. [6]

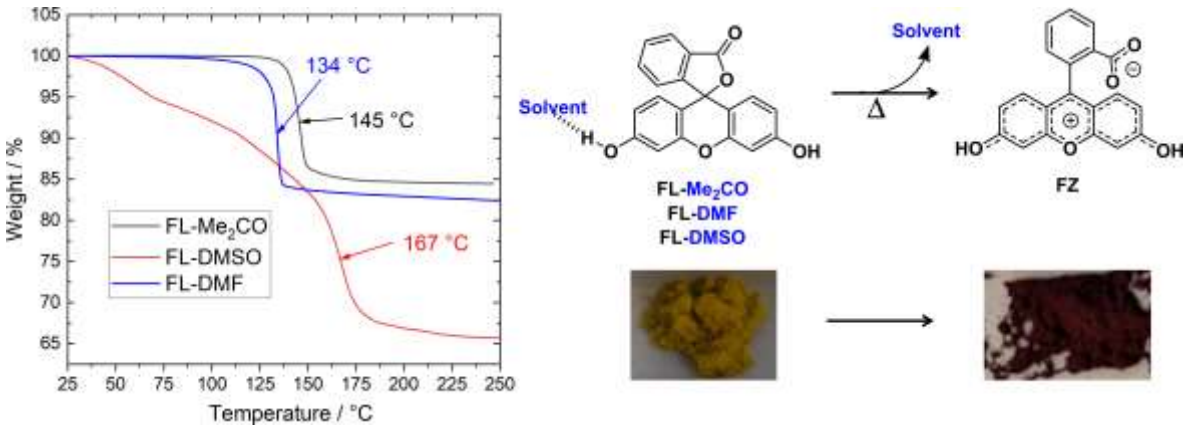

Figure S27. Thermogravimetric analyses (under air, 5 °Cmin^{-1}) for the **FL** solvates, displaying a thermal transition around 134 – 167 °C, associated with the loss of solvent and a clear change in color from yellow to red due to the concomitant tautomerization of **FL** to the quinoid tautomer (**FQ**).

S7. X-Ray Diffraction Studies

Crystals of **FL** and of the **FL-MeCN** solvate were grown by slow diffusion evaporation of a saturated solution of the **FL-Me$_2$CO** solvate in acetonitrile. Data were collected on a Bruker Kappa Apex II diffractometer equipped with a 30 W air-cooled microfocus source using MoK_α radiation ($\lambda = 0.71073$ Å) and on a Rigaku XtaLAB Synergy Dualflex diffractometer using a PhotonJet X-ray source (CuK_α, $\lambda = 1.54184$ Å). An Oxford Cryosystems Cryostream cooling device was used to collect the data at low temperature (100(2) K). Phi and Omega scans were performed for data collection, an empirical absorption correction was applied and the structures were solved by intrinsic phasing method (ShelXT). [11] All reflection data set were corrected for Lorentz and polarization effects. The first structure solution was obtained using the SHELXS-2018 program and the SHELXL-2018 was applied for refinement and output data. [12] All non-hydrogen atoms were found by Fourier map difference and refined anisotropically. [13] All the hydrogen atoms were refined isotropically at calculated positions using a riding model. All software manipulations were performed through the ShelXle program. [14] Mercury 3.7 and ORTEP-3 were used to prepare artwork representations. [15] Deposition Numbers 2407098-2407099 contain the supplementary crystallographic data for this paper. These data are provided free of charge by the joint Cambridge Crystallographic Data Centre and Fachinformationszentrum Karlsruhe Access Structures service.

Table S2. Crystal Structure and Refinement Data

	FL	**FL-MeCN**
formula	$C_{20}H_{12}O_5$	$C_{20}H_{12}O_5$, CH_3CN
temperature (K)	100(2)	100(2)
crystal system	monoclinic	monoclinic
space group	$P2_1/c$	$P2_1/c$
a (Å)	12.84670(10)	7.379(5)
b (Å)	9.54310(10)	15.617(10)
c (Å)	12.05780(10)	14.777(10)
α (deg)	90	90
β (deg)	94.8450(10)	96.00(2)
γ (deg)	90	90
volume (Å^3)	1472.97(2)	1693.4(19)
Z	4	4
Density (g·cm^{-3})	1.498	1.464
Crystal size (mm)	0.2 x 0.2 x 0.1	0.20 x 0.16 x 0.06
θ range (deg)	3.453 - 79.929	1.903 - 35.615
reflns collected/ unique (Rint)	29806 / 3189 (0.0461)	81375 / 7495 (0.0486)
final *R* indices [$I > 2\sigma(I)$]	$R_1 = 0.0395$	$R_1 = 0.0415$
	w$R_2 = 0.1025$	w$R_2 = 0.1136$
R indices (all data)	$R_1 = 0.0422$	$R_1 = 0.0518$
	w$R_2 = 0.1064$	w$R_2 = 0.1211$

$R = \Sigma||F_o| - |F_c||/ \Sigma |F_o|$. $wR_2 = [\Sigma[w(F_o^2 - F_c^2)^2] / \Sigma [w(F_o^2)^2]]^{1/2}$.

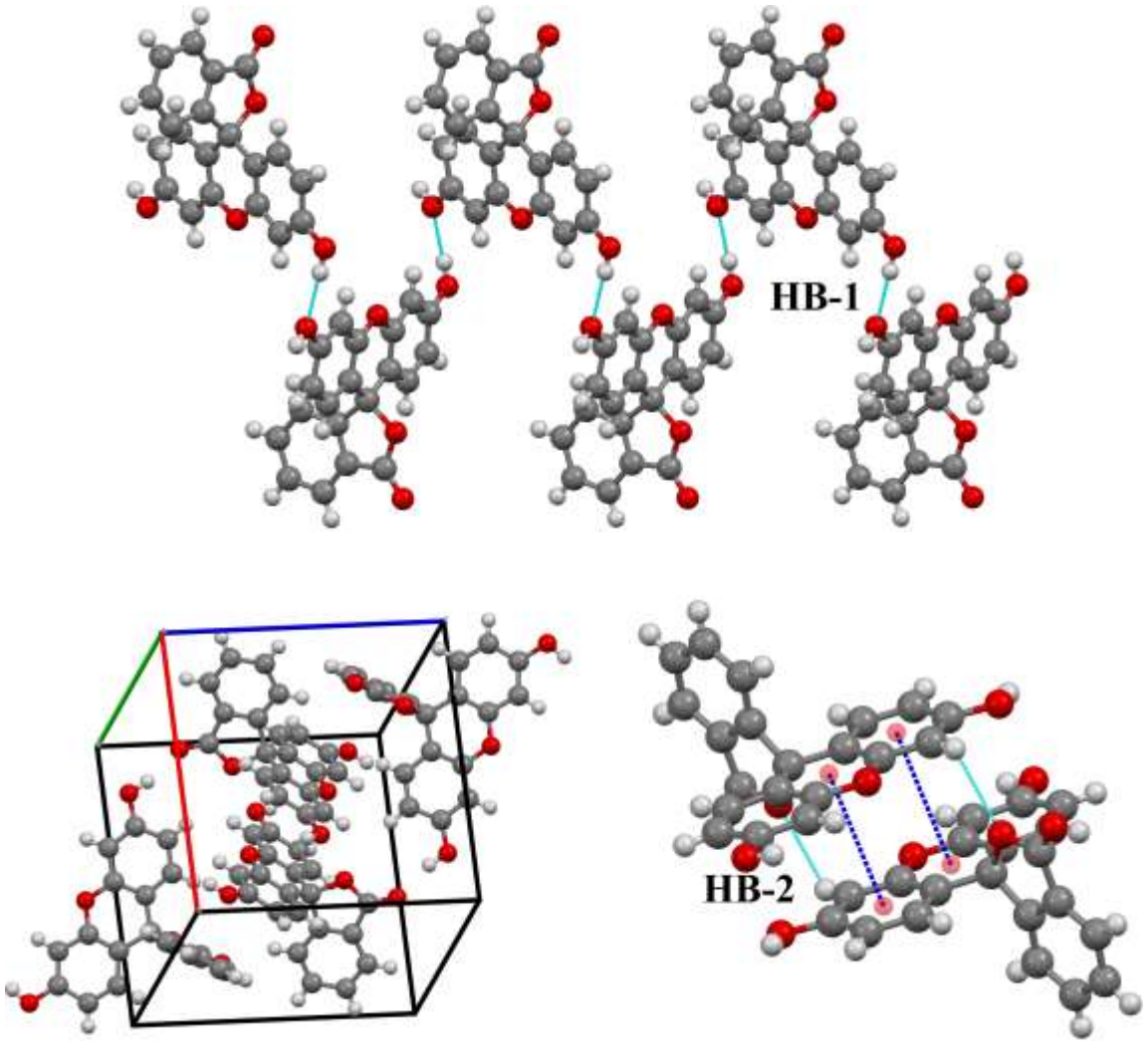

Figure S28. Crystallographic projections for **FL**, showing selected relevant supramolecular interactions. Hydrogen bonds (HB) are drawn in turquoise and π-interactions in blue. Relevant bond lengths [Å] and angles [°]. For HB-1: O3-H5 1.98, O3-H5-O1 174. For HB-2: O4-H4' 2.55, O4-H4'-C4' 123. For the π-interaction the intercentroid distance is 3.709 Å.

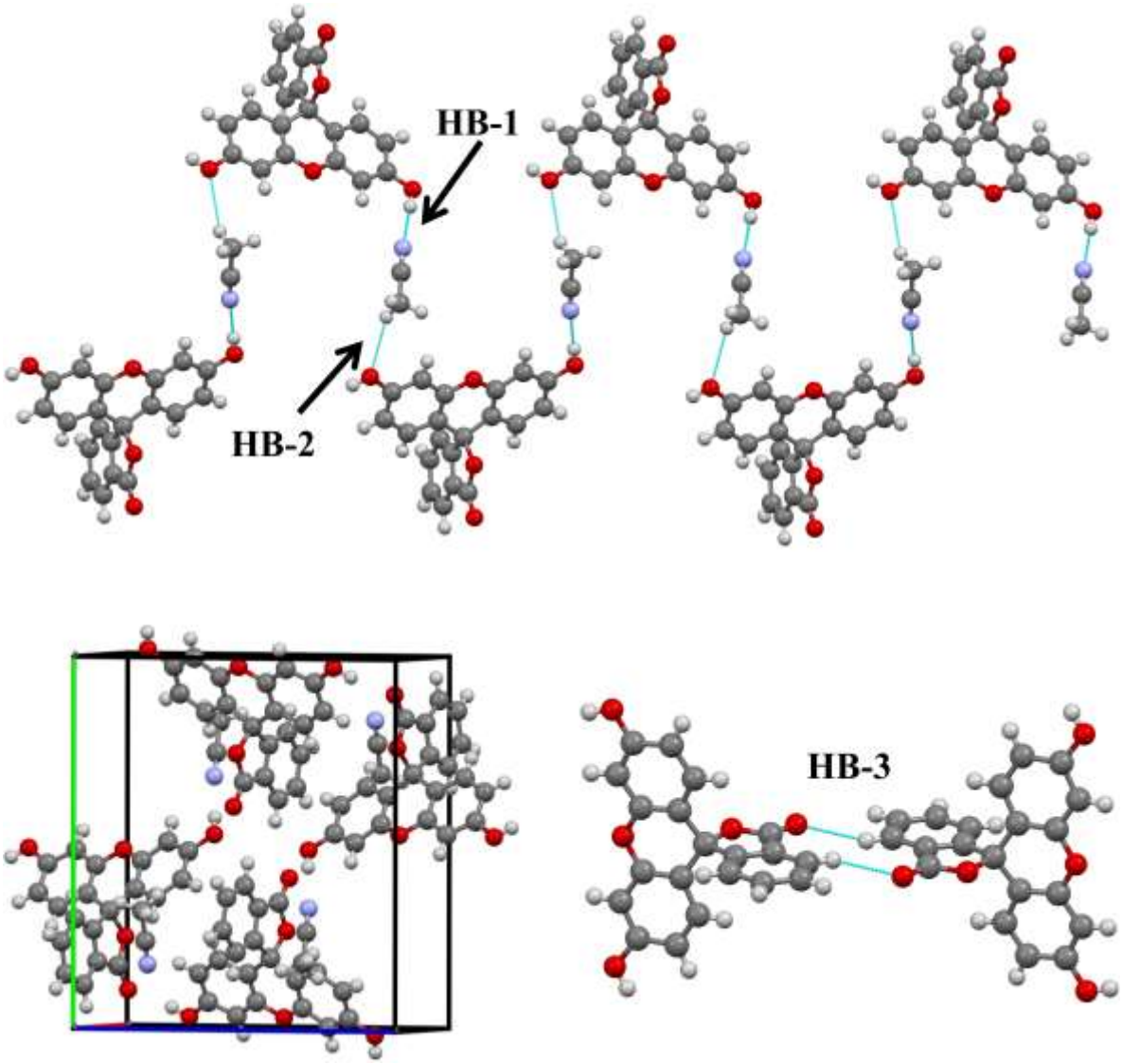

Figure S29. Crystallographic projections for **FL-MeCN** showing selected relevant hydrogen bonds (HB) in turquoise. Relevant bond lengths [Å] and angles [°]. For HB-1: N1-H3A 2.00, N1-H3A-O3 177. For HB-2: O1-H16B 2.68, O1-H16B-O1 145. For HB-3: O5-H12 2.46, O5-H12-O5 157.

S8. NMR Spectroscopy

NMR spectra were recorded on Bruker Avance III 300 and 600 MHz spectrometers using deuterated solvents and standard pulse sequences; chemical shifts for ^{1}H- and ^{13}C-NMR data are relative to the residual nondeuterated solvent signal, fixed at δ = 1.940 (CD_3CN), 2.840 (Acetone-d_6), 2.500 (DMSO-d_6) and 3.310 (CD_3OD) for ^{1}H-NMR and δ = 1.320 (CD_3CN), 39.520 (DMSO-d_6), 29.840 (Acetone-d_6) and 49.000 (CD_3OD) ppm for ^{13}C-NMR. Chemical shifts are given in ppm with multiplicities abbreviated as singlet (s), doublet (d), triplet (t), doublet of doublets (dd), doublet of doublets of doublets (ddd), triplet of doublets (td) and multiplet (m). The assignment of the NMR signals was performed with the aid of 2D-NMR techniques, including homonuclear (^{1}H-^{1}H) COSY/NOESY and heteronuclear (^{1}H-^{13}C) HSQC/HMBC experiments. Ambiguity found during the assignment of quaternary carbons was circumvented employing DFT (GIAO) computations of the ^{13}C-NMR spectrum at the M06-2X/6-31+G(d,p)/PCM level of theory as described in Section S3.

NMR characterization for FL

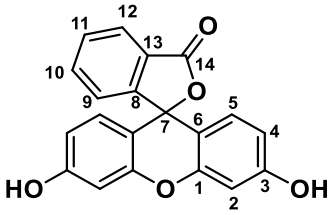

All the data presented here for this tautomer were recorded from freshly prepared analytical samples of the compound as an acetone solvate (**FL-Me$_2$CO**). Equivalent results were obtained when the NMR spectra were recorded dissolving commercial red fluorescein (**FQ**) in acetone-d_6 or DMSO-d_6. The NMR studies showed the exclusive presence of the **FL** tautomer, characterized by the C_2 symmetry expected for this species, and by the various characteristic signals, such as the lactone carbonyl and the spirocyclic carbon that resonated at δ = 168.76 to 170.10 ppm and δ = 83.08 to 83.92 ppm, respectively

^{1}H NMR (300 MHz, CD_3CN) δ 8.00 – 7.94 (m, 1H, H-12), 7.78 – 7.64 (m, 2H, H-10/H-11), 7.47 (s, 2H, OH), 7.19 (d, J = 7.6 Hz, 1H, H-9), 6.75 – 6.51 (m, 6H, H-2/H-5/H-4). **^{13}C-NMR** (75 MHz, CD_3CN) δ 170.10 (C-14), 159.90 (C-3), 154.03 (C-8), 153.27 (C-1), 136.30 (C-10), 130.87 (C-11), 130.32 (C-5), 127.61 (C-13), 125.58 (C-12), 124.85 (C-9), 113.26 (C-4), 111.81 (C-6), 103.42 (C-2), 83.92 (C-7).

^{1}H NMR (300 MHz, Acetone-d_6) 9.00 (s, 2H, OH), 7.98 (ddd, J = 7.4, 1.3, 0.8 Hz, 1H, H-12), 7.84 – 7.77 (m, 1H, H-10), 7.72 (td, J = 7.4, 1.1 Hz, 1H, H-11), 7.30 – 7.26 (m, 1H, H-9), 6.76 (dd, J = 2.2, 0.7 Hz, 2H, H-2), 6.68 – 6.60 (m, 4H, H-4/H-5). **^{13}C-NMR** (75 MHz, Acetone-d_6) δ 169.51 (C-

14), 160.24 (C-3), 153.96 (C-8), 153.32 (C-1), 136.01 (C-10), 130.70 (C-11), 130.13 (C-5), 127.83 (C-13), 125.32 (C-12), 124.89 (C-9), 113.26 (C-4), 111.65 (C-6), 103.31 (C-2), 83.66 (C-7).

^{1}H NMR (300 MHz, DMSO-d_6) δ 10.14 (s, 2H, OH), 7.99 (ddd, J = 7.5, 1.3, 0.8 Hz, 1H, H-12), 7.79 (td, J = 7.5, 1.3 Hz, 1H, H-10), 7.71 (td, J = 7.4, 1.1 Hz, 1H, H-11), 7.30 – 7.23 (m, 1H, H-9), 6.68 (t_{app}, J = 1.3 Hz, 2H, H-2), 6.54 (d_{app}, J = 1.5 Hz, 4H, H-4/H-5). **^{13}C-NMR** (75 MHz, DMSO-d_6) δ 168.76 (C-14), 159.50 (C-3), 152.49 (C-8), 151.87 (C-1), 135.62 (C-10), 130.09 (C-11), 129.09 (C-5), 126.19 (C-13), 124.62 (C-12), 124.06 (C-9), 112.63 (C-4), 109.59 (C-6), 102.25 (C-2), 83.08 (C-7).

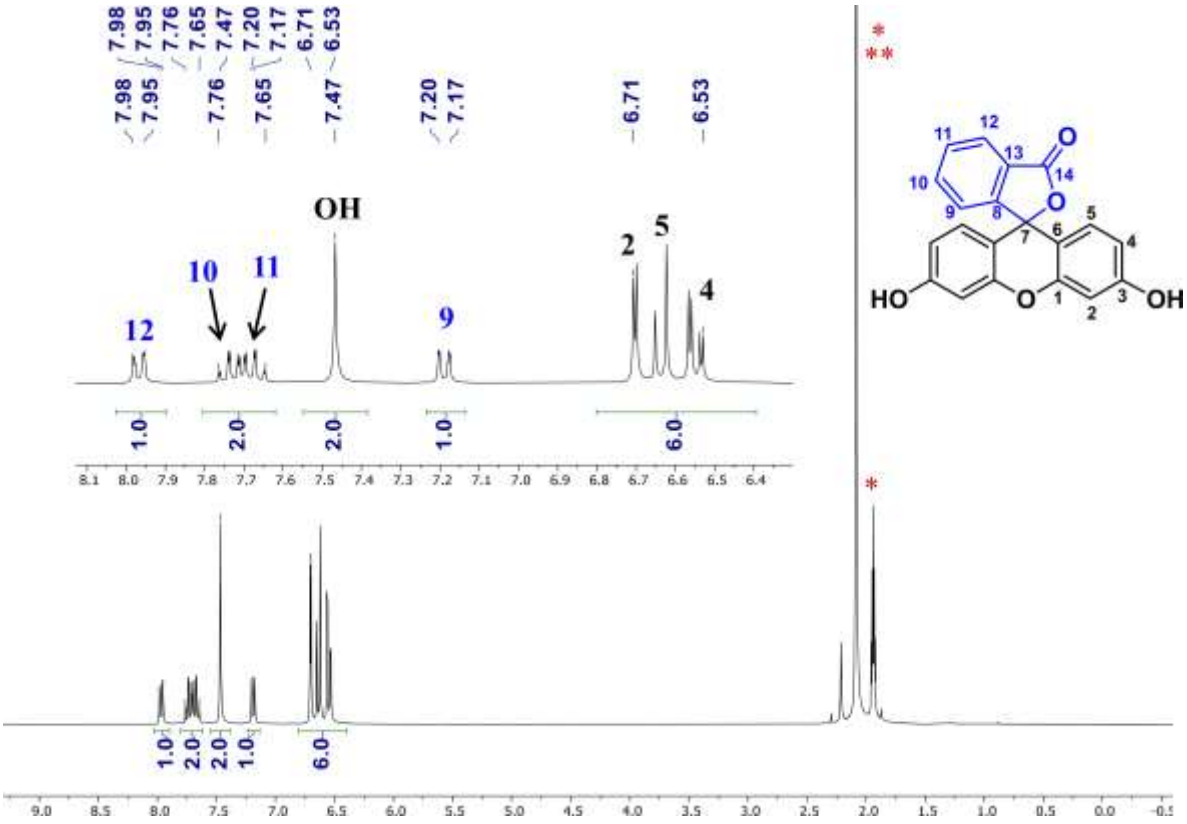

Figure S30. ^{1}H-NMR [300 MHz] spectrum for the lactoid tautomer of fluorescein (**FL**) in CD_3CN. The spectrum was recorded from a freshly prepared analytical sample of the compound as an acetone solvate (**FL-Me$_2$CO**). Signals marked with * and ** correspond to residual nondeuterated solvents or to the acetone from the **FL-Me$_2$CO** solvate, respectively.

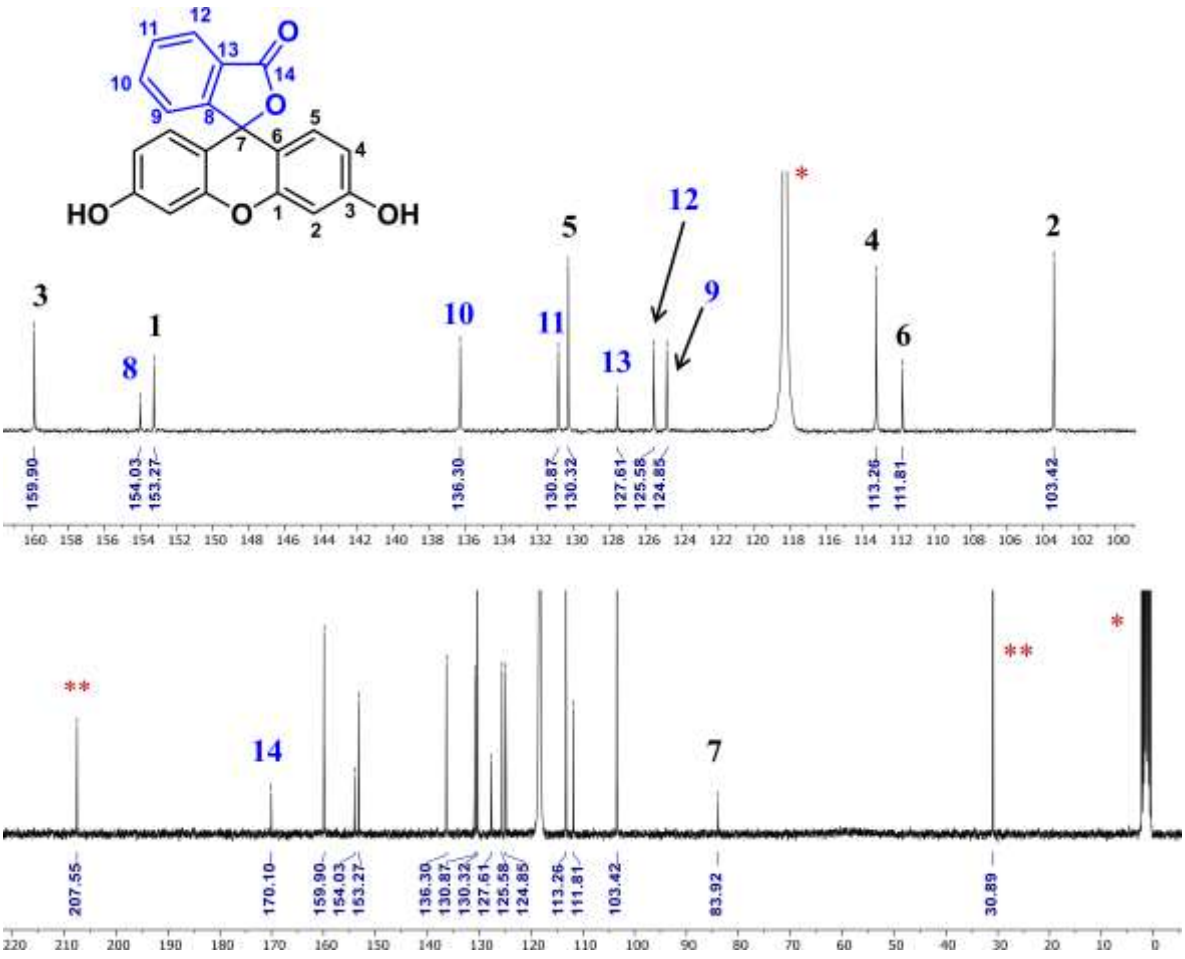

Figure S31. ^{13}C-NMR [75 MHz] spectrum for the lactoid tautomer of fluorescein (**FL**) in CD_3CN. The spectrum was recorded from a freshly prepared analytical sample of the compound as an acetone solvate (**FL-Me$_2$CO**). Signals marked with * and ** correspond to residual nondeuterated solvents or to the acetone from the **FL-Me$_2$CO** solvate, respectively.

NMR Characterization for FZ

The analyses leading to the characterization of **FZ** were performed using commercial red quinoid fluorescein (**FQ**). Although intuition suggests that directly dissolving **FQ** would allow access to the same tautomer in solution, this was not the case. NMR analyses in acetone-d_6 and DMSO-d_6, where FQ is very soluble, led to analogous results to those observed for the **FL-Me$_2$CO** solvate (*vide supra*), suggesting that in these solvents a fast **FQ**$\rightarrow$**FL** tautomerization occurs. In CD_3OD, however, the results were strikingly different, where a temperature dependence of the NMR spectra was observed. This is shown in Supplementary Figure S32 where at T = 183 K the ^{13}C-NMR spectrum shows the exclusive presence of the **FL** tautomer, with the characteristic signal of the spirocyclic carbon C-7 resonating at δ = 84.09 ppm, while at T $\geq$ 298 K the **FL** tautomer is completely absent, indicating a tautomerization towards either **FQ** or **FZ**. We assigned the product as the **FZ** tautomer on the basis of the clear C_2 symmetry retained by the fluorophore in both the ^{13}C-NMR spectra and the corresponding ^{1}H-NMR spectra (Supplementary Figure S33). Importantly, signals corresponding to carbons C-3, C-7 and C-8 in the NMR spectrum of **FZ** are broadened or absent, indicating a fast chemical exchange.

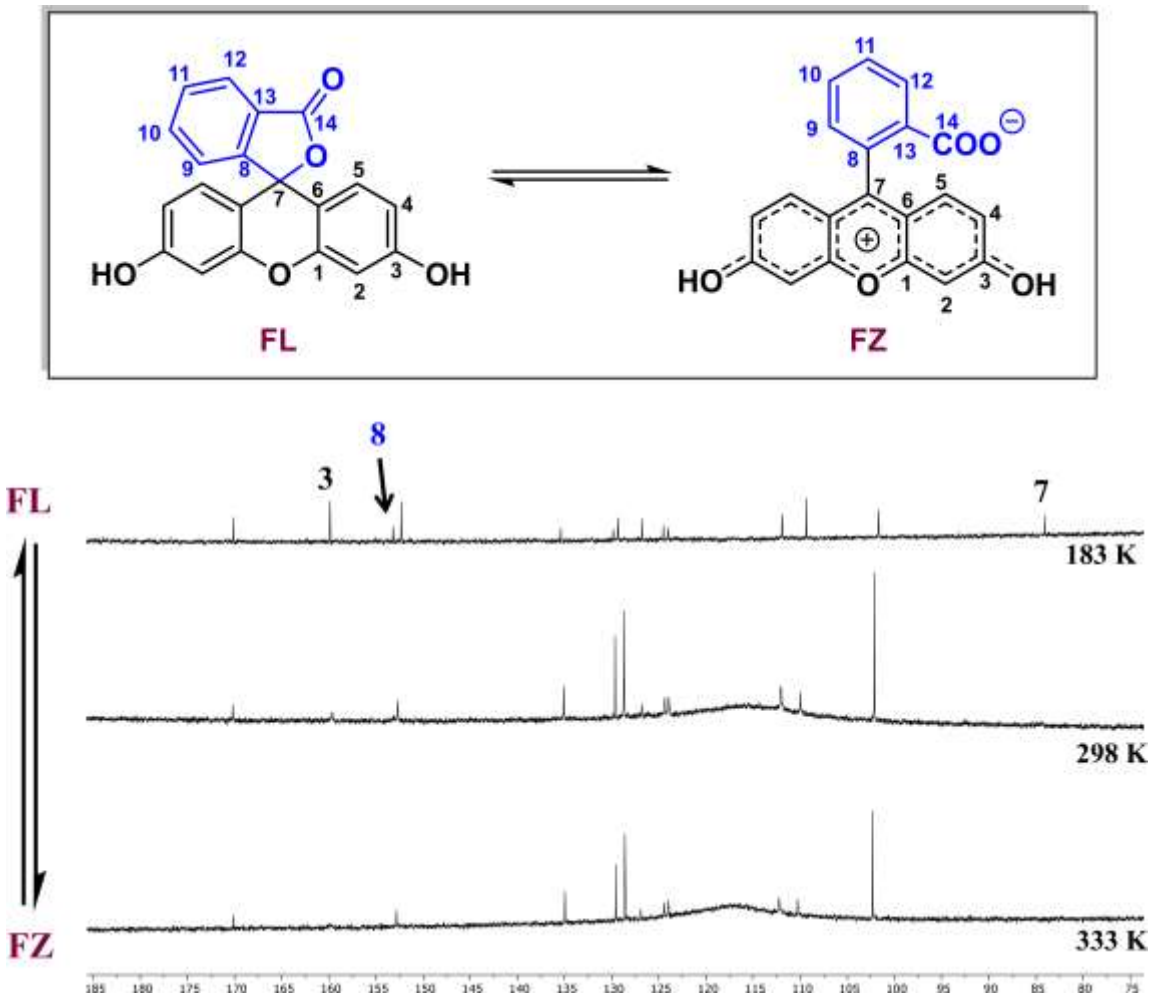

Figure S32. Variable-temperature ^{13}C-NMR spectra at 150 MHz for a sample of red fluorescein (**FQ**) in CD_3OD, showing the equilibrium stablished between the lactoid (**FL**) and the zwitterionic (**FZ**) tautomers. For clarity, only selected signals affected by a rapid exchange are assigned.

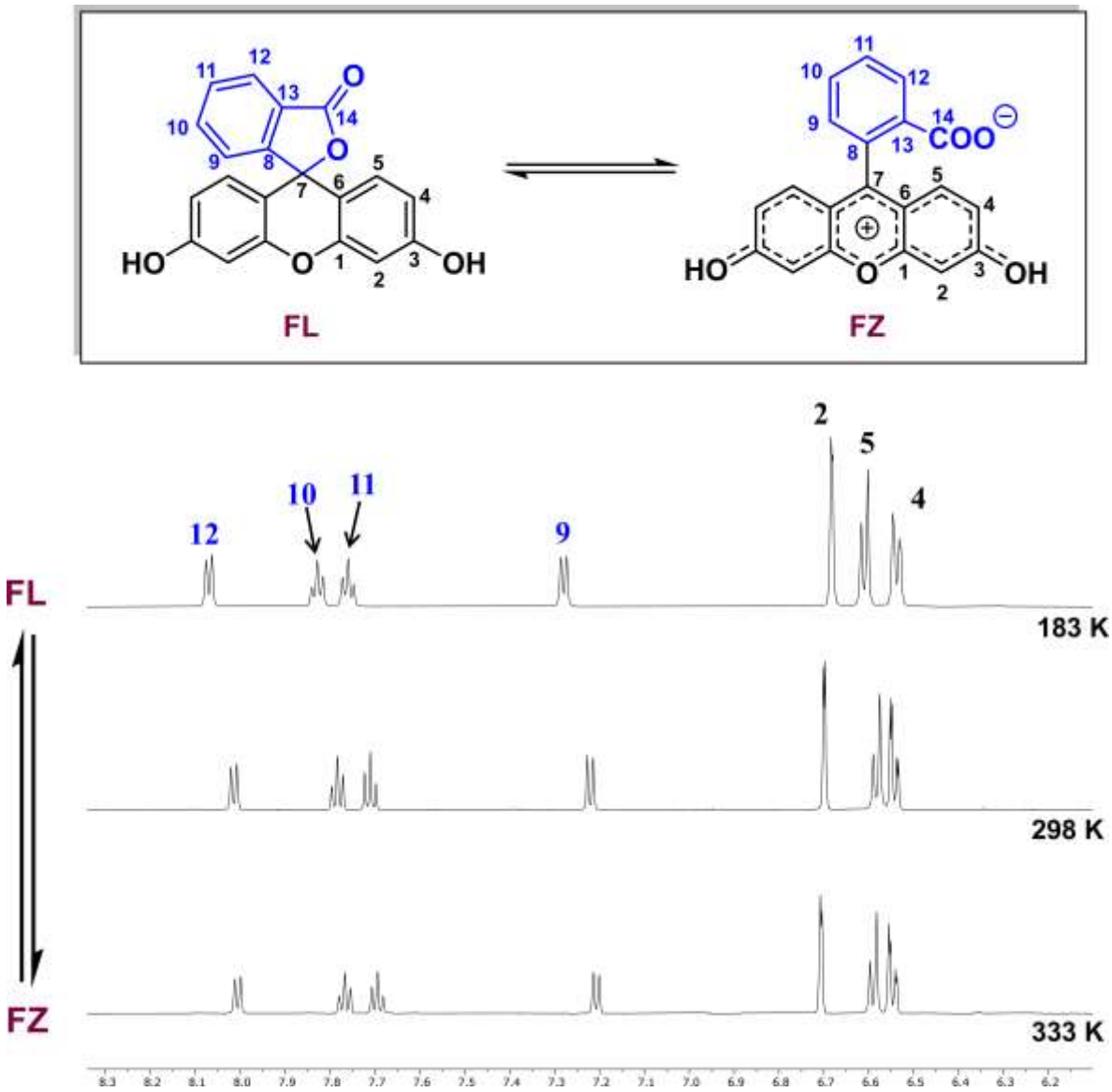

Figure S33. Variable-temperature ^{1}H-NMR spectra at 600 MHz for a sample of red fluorescein (**FQ**) in CD_3OD, showing the equilibrium stablished between the lactoid tautomer (**FL**) and the zwitterionic tautomer (**FZ**).

S9. References

[1] E. M. Espinoza, J. A. Clark, J. Soliman, J. B. Derr, M. Morales, V. I. Vullev, Practical Aspects of Cyclic Voltammetry: How to Estimate Reduction Potentials When Irreversibility Prevails, *J. Electrochem. Soc.* **2019**, *166*, H3175-H3187.

[2] D. M. de Leeuw, M. M. J. Simenon, A. R. Brown, R. E. F. Einerhand, Stability of N-Type Doped Conducting Polymers and Consequences for Polymeric Microelectronic Devices, *Synth. Met.* **1997**, *87*, 53-59.

[3] J. Panchompoo, L. Aldous, M. Baker, M. I. Wallace, R. G. Compton, One-step synthesis of fluorescein modified nano-carbon for Pd(ii) detection via fluorescence quenching, *Analyst* **2012**, *137*, 2054-2062.

[4] Gaussian 16, Revision B.01. M. J. Frisch, G. W. Trucks, H. B. Schlegel, G. E. Scuseria, M. A. Robb, J. R. Cheeseman, G. Scalmani, V. Barone, G. A. Petersson, H. Nakatsuji, X. Li, M. Caricato, A. V. Marenich, J. Bloino, B. G. Janesko, R. Gomperts, B. Mennucci, H. P. Hratchian, J. V. Ortiz, A. F. Izmaylov, J. L. Sonnenberg, D. Williams-Young, F. Ding, F. Lipparini, F. Egidi, J. Goings, B. Peng, A. Petrone, T. Henderson, D. Ranasinghe, V. G. Zakrzewski, J. Gao, N. Rega, G. Zheng, W. Liang, M. Hada, M. Ehara, K. Toyota, R. Fukuda, J. Hasegawa, M. Ishida, T. Nakajima, Y. Honda, O. Kitao, H. Nakai, T. Vreven, K. Throssell, J. A. Montgomery, Jr., J. E. Peralta, F. Ogliaro, M. J. Bearpark, J. J. Heyd, E. N. Brothers, K. N. Kudin, V. N. Staroverov, T. A. Keith, R. Kobayashi, J. Normand, K. Raghavachari, A. P. Rendell, J. C. Burant, S. S. Iyengar, J. Tomasi, M. Cossi, J. M. Millam, M. Klene, C. Adamo, R. Cammi, J. W. Ochterski, R. L. Martin, K. Morokuma, O. Farkas, J. B. Foresman, and D. J. Fox, Gaussian, Inc., Wallingford CT, 2016.

[5] (a)Y. Zhao, D. G. Truhlar, The M06 suite of density functionals for main group thermochemistry, thermochemical kinetics, noncovalent interactions, excited states, and transition elements: two new functionals and systematic testing of four M06-class functionals and 12 other functionals, *Theor. Chem. Acc.* **2008**, *120*, 215-241; (b) M. E. Ochoa, P. Labra-Vázquez, N. Farfán, R. Santillan, Designed Synthesis and Crystallization of Isomorphic Molecular Gyroscopes with Cell-like Bilayer Self-Assemblies, *Cryst. Growth Des.* **2018**, *18*, 2795-2803.

[6] A. P. Scott, L. Radom, Harmonic Vibrational Frequencies: An Evaluation of Hartree-Fock, Moller-Plesset, Quadratic Configuration Interaction, Density Functional Theory, and Semiempirical Scale Factors, *J. Phys. Chem.* **1996**, *100*, 16502-16513.

[7] I. A. Sheikh, Stereoselectivity and the potential endocrine disrupting activity of di-(2-ethylhexyl)phthalate (DEHP) against human progesterone receptor: a computational perspective, *J. Appl. Toxicol.* **2016**, *36*, 741-747.

[8] A. D. Laurent, D. Jacquemin, TD-DFT benchmarks: A review, *Int. J. Quantum Chem.* **2013**, *113*, 2019-2039.

[9] (a) L. Mosca, R. S. Khnayzer, M. S. Lazorski, E. O. Danilov, F. N. Castellano, P. Anzenbacher Jr., Sensing of 2,4,6-Trinitrotoluene (TNT) and 2,4-Dinitrotoluene (2,4-DNT) in the Solid State with Photoluminescent RuII and IrIII Complexes, *Chem. Eur. J.* **2015,** *21*, 4056-4064; (b) K. Zhang, H. Zhou, Q. Mei, S. Wang, G. Guan, R. Liu, J. Zhang, Z. Zhang, Instant Visual Detection of Trinitrotoluene Particulates on Various Surfaces by Ratiometric Fluorescence of Dual-Emission Quantum Dots Hybrid, *J. Am. Chem. Soc.* **2011,** *133*, 8424-8427.

[10] M. Arhangelskis, M. D. Eddleston, D. G. Reid, G. M. Day, D.-K. Bučar, A. J. Morris, W. Jones, Rationalization of the Color Properties of Fluorescein in the Solid State: A Combined Computational and Experimental Study, *Chem. Eur. J.* **2016**, *22*, 10065-10073.

[11] G. Sheldrick, SHELXT – Integrated space-group and crystal-structure determination, *Acta Crystallogr. A* **2015**, *71*, 3-8.

[12] G. Sheldrick, A short history of SHELX, *Acta Crystallogr. A* **2008**, *64*, 112-122.
[13] P. W. Betteridge, J. R. Carruthers, R. I. Cooper, K. Prout, D. J. Watkin, CRYSTALS version 12: software for guided crystal structure analysis, *J. Appl. Crystallogr.* **2003**, *36*, 1487.
[14] C. B. Hubschle, G. M. Sheldrick, B. Dittrich, *J. Appl. Crystallogr.* **2011**, *44*, 1281-1284.
[15] (a) C. F. Macrae, P. R. Edgington, P. McCabe, E. Pidcock, G. P. Shields, R. Taylor, M. Towler, J. van de Streek, Mercury: visualization and analysis of crystal structures, *J. Appl. Crystallogr.* **2006**, *39*, 453-457; (b) L. Farrugia, ORTEP-3 for Windows - a version of ORTEP-III with a Graphical User Interface (GUI), *J. Appl. Crystallogr.* **1997**, *30*, 565.